
















Sub-surface Imaging of Porous GaN Distributed Bragg Reflectors via Backscattered Electrons

Maruf Sarkar^{1,*}, Francesca Adams¹, Sidra A. Dar¹, Jordan Penn², Yihong Ji¹,
Abhram Gundimeda¹, Tongtong Zhu³, Chaowang Liu⁴, Hassan Hirshy⁴,
Fabien C.-P. Massabuau⁵, Thomas O'Hanlon⁶, Menno J. Kappers¹, Saptarsi Ghosh¹,
Gunnar Kusch¹, and Rachel A. Oliver¹

¹Department of Materials Science and Metallurgy, University of Cambridge, Cambridge CB3 0FS, UK

²Department of Physics, University of Oxford, Oxford OX1 3PJ, UK

³Poro Technologies Ltd, Sawston CB22 3JH, UK

⁴IQE Europe Limited, Cardiff CF3 0LW, UK

⁵Department of Physics, University of Strathclyde, Glasgow G4 0NG, UK

⁶Plymouth Electron Microscopy Center, University of Plymouth, Plymouth PL4 8AA, UK

*Corresponding author: Maruf Sarkar, E-mail: maamms2@cam.ac.uk

Abstract

In this article, porous GaN distributed Bragg reflectors (DBRs) were fabricated by epitaxy of undoped/doped multilayers followed by electrochemical etching. We present backscattered electron scanning electron microscopy (BSE-SEM) for sub-surface plan-view imaging, enabling efficient, non-destructive pore morphology characterization. In mesoporous GaN DBRs, BSE-SEM images the same branching pores and Voronoi-like domains as scanning transmission electron microscopy. In microporous GaN DBRs, micrographs were dominated by first porous layer features (45 nm to 108 nm sub-surface) with diffuse second layer (153 nm to 216 nm sub-surface) contributions. The optimum primary electron landing energy (LE) for image contrast and spatial resolution in a Zeiss GeminiSEM 300 was approximately 20 keV. BSE-SEM detects porosity ca. 295 nm sub-surface in an overgrown porous GaN DBR, yielding low contrast that is still first porous layer dominated. Imaging through a ca. 190 nm GaN cap improves contrast. We derived image contrast, spatial resolution, and information depth expectations from semi-empirical expressions. These theoretical studies echo our experiments as image contrast and spatial resolution can improve with higher LE, plateauing towards 30 keV. BSE-SEM is predicted to be dominated by the uppermost porous layer's uppermost region, congruent with experimental analysis. Most pertinently, information depth increases with LE, as observed.

Key words: backscattered electrons (BSEs), distributed Bragg reflectors (DBRs), porous gallium nitride, scanning electron microscopy (SEM), sub-surface imaging

Introduction

Introducing porosity into GaN offers a non-compositional degree of freedom to adjust the properties of this critical optoelectronic material, opening up novel design space for device engineering (Griffin & Oliver, 2020; Yao et al., 2023). Porous nitride semiconductors exhibit many material properties distinct from monolithic nitride layers. Porosity has been demonstrated to allow the engineering of strain relaxation (Yang et al., 2019), optical birefringence (Elafandy et al., 2021) and, most pertinently to this work, refractive index contrast (Zhang et al., 2015).

Porous GaN distributed Bragg reflectors (DBRs) are typically fabricated by doping-selective electrochemical etching (ECE) (Tseng et al., 2014). Two common approaches allow the etchant to access sub-surface doped layers. In the first, a dielectric layer (SiO_x or SiN_x) protects the surface and deep trenches defined by lithographic techniques provide an etchant access route (Mishkat-Ul-Masabih et al., 2018). The DBRs investigated here are made by a more recently developed approach, in which the GaN surface is left unprotected, and

the etchant accesses doped layers via the etched cores of intrinsic threading dislocations (Zhu et al., 2017; Massabuau et al., 2020a). Porous GaN DBRs have been fabricated using this latter technique with a top surface suitable for LED overgrowth (Jarman et al., 2019). The resulting porosity is determined by epitaxial structure, doping density, electro-oxidation potential, and defect density (Griffin & Oliver, 2020).

Porous GaN DBRs are effectively a GaN/air composite where the selective introduction of porosity periodically reduces the GaN refractive index to achieve Bragg-condition reflectivity (Springbett et al., 2018). For a fixed number of periods, increased reflectivity may be achieved by increasing the refractive index contrast, i.e. by increasing the porosity (Zhao et al., 2020). However, it is essential to preserve DBR periodicity with sharply defined interfaces and ensure that the pores' size remains lower than the wavelength of light in the material to minimize diffuse scattering (Park et al., 2013). Porous GaN DBRs have been shown to improve the light extraction efficiency from overgrown LEDs (Jarman et al., 2019). These mirrors can also create resonant cavities

Received: October 13, 2023. Revised: February 9, 2024. Accepted: March 4, 2024

© The Author(s) 2024. Published by Oxford University Press on behalf of the Microscopy Society of America.

This is an Open Access article distributed under the terms of the Creative Commons Attribution License (<https://creativecommons.org/licenses/by/4.0/>), which permits unrestricted reuse, distribution, and reproduction in any medium, provided the original work is properly cited.

for vertical-cavity surface-emitting laser devices (Lee et al., 2015; Palmquist et al., 2023) and single photon sources (Springbett et al., 2018).

Cross-sectional scanning electron microscopy (SEM) provides a limited view of the pore structure along the growth direction (Shiu et al., 2016). This approach facilitates prompt characterization in studies of changing epitaxial or etching parameters (Zhao et al., 2022). However, cleaving as an approach to sample preparation often struggles to produce a planar cross-section (Griffin et al., 2019), free of cleavage steps (Griffin et al., 2018), or debris (Liu et al., 2020). While such measurements are reported frequently, less routine imaging in the plan-view orientation can provide better access to ECE uniformity. Likewise, this perspective may improve the characterization of competing etch pathways, allowing access to pores formed at the onset of crystallographic defect-mediated ECE (Griffin et al., 2020).

One approach to imaging the plan-view sub-surface morphology of such DBRs is to use transmission electron microscopy (TEM) (Massabuau et al., 2020a). A recently demonstrated sequential methodology by Massabuau et al. (2020b) consisted of front-side Ar⁺ milling followed by plan-view annular dark field (ADF) imaging, repeating in iteration to image multiple sub-surface porous layers. This approach can image single porous DBR layers, but it is sample-destructive and requires specialized training and non-trivial time investment.

A technique for reconstructing the plan-view sub-surface morphology is focused ion beam scanning electron microscopy (FIB-SEM) tomography (Griffin et al., 2020). Through FIB serial sectioning, 2D SEM imaging, and 3D image reconstruction, one can map 3D nanostructure from a series of 2D sections (Cantoni & Holzer, 2014). However, collecting a tomographic dataset requires a time investment that can scale from hours to days (Xu et al., 2017). Naturally, the act of serial sectioning is inherently a destructive one. Lastly, image processing, tomograph rendering, and porosity segmentation also require specialized training as well as computational infrastructure (Makovetsky et al., 2018).

A successful application of tomography to porous GaN DBRs is the study of birefringence by Griffin et al. (2020). The artifact that most affects the tomographic FIB-SEM of such porous media is the pore-back effect, where additional secondary electron (SE) signal, not directly attributed to the section plane, is generated inside the pores (Reimers et al., 2019). Therefore, their reconstructions were most successful when the pores were aligned along a common direction, roughly perpendicular to the surfaces from which the 2D SEM images were recorded, reducing non-topological artifacts (Ke et al., 2023).

Therefore, we propose using backscattered electron (BSE) imaging in the SEM as a rapid, wide field of view (FOV), and non-destructive alternative to the above-established techniques to image *sub-surface* GaN DBR porosity in plan-view (Wei et al., 2020). We will demonstrate that our proposed method can efficiently assess the impact of changing etch conditions on the pore morphology. BSE-SEM is widely used to characterize cross-sectional nitride samples (Shiojiri et al., 2006; Garitagoitia Cid et al., 2018) and has been applied in the previously mentioned routine characterization of porous GaN DBRs by examining cleaved cross-sections (Jarman et al., 2019). These studies demonstrate the potential for high contrast between pores and GaN that arises from the inherent Z-contrast-dominated image formation mechanism (Goldstein et al., 2017). Here, we investigate how BSE imaging

parameters can be adjusted to allow optimization of image contrast and spatial resolution of porous GaN DBRs and explore the information depth achieved in this imaging modality.

Materials

To fabricate the investigated porous GaN DBRs, periodic multilayers consisting of alternating non-intentionally doped (NID) GaN and conductive Si-doped GaN layers were grown by metal-organic vapor phase epitaxy (MOVPE). Then, the as-grown wafers were etched in a 0.25 M oxalic acid electrolyte, with threading dislocations acting as the channels for the etchant to access Si-doped layers, which are selectively etched (Zhu et al., 2017; Massabuau et al., 2020a).

Firstly, we studied porous DBRs based on epitaxial structures comprising 15 pairs of 45 nm NID GaN and 63 nm Si-doped ($>10^{19} \text{ cm}^{-3}$) GaN, grown upon c-plane sapphire substrates; a schematic of the as-grown DBR layers is depicted in Figure 1a. These wafers were grown and etched by Poro Technologies Ltd (Porotech). Two such wafers were grown, targeting reflection in visible blue wavelengths. However, they were etched at different voltages, which we label V_0 (for the lower etching voltage) and $V_0 + 5 \text{ V}$ (for the second DBR etched at a voltage 5 V above the original DBR). BSE-SEM of these DBRs will first be compared against other microscopy techniques and, later, will be quantified in terms of spatial resolution and image contrast.

Secondly, we examined another porous DBR comprising five pairs of 45 nm NID GaN and 63 nm Si-doped ($>10^{19} \text{ cm}^{-3}$) GaN grown upon a silicon substrate. The as-grown epilayers undergo the above ECE. Afterwards, the as-etched DBR is overgrown by MOVPE with $1 \mu\text{m}$ of NID GaN to emulate LED overgrowth. However, this overgrowth is not fully optimized. A schematic of the as-grown DBR layers is depicted in Figure 1b. This structure was grown by IQE PLC and etched by Porotech. This DBR will aid in characterizing the depth limits of the information obtained with BSE-SEM.

Methods

SEM was performed in a Zeiss GeminiSEM 300, operating at primary electron landing energies (LE) of 2–25 keV (Crouzier et al., 2021). SE-SEM was captured with the in-column detector, and BSE-SEM was captured with the BSD4 annular detector. The BSD4 consists of a diode array divided into five segments (Zeiss, 2013). Four quadrants comprise the main ring, with a fifth segment placed behind the ring, closer to the retractable arm. The segments can function in a “COMPO” mode whereby the signal from each segment is added to the total. This is the mode of operation used throughout.

Cross-sectional and tomographic FIB-SEM were performed in a Zeiss Crossbeam 540. Ion milling was conducted with a 30 kV Ga⁺ ion beam; images were captured with the in-column SE detector. Tomographic dataset reconstruction was conducted in ORS Dragonfly 2022.2 (Object Research Systems, Montreal, Canada). Rigid body image registration of tomographs was performed using the StackReg ImageJ2 plugin (Thevenaz et al., 1998).

Scanning transmission electron microscopy (STEM) was performed in an aberration-corrected FEI Titan³, operating at a 300 kV acceleration voltage. Images were captured with a high-angle annular dark-field (HAADF) detector. Atomic force microscopy (AFM) was performed in a Bruker Dimension Icon AFM in PeakForce Tapping mode using

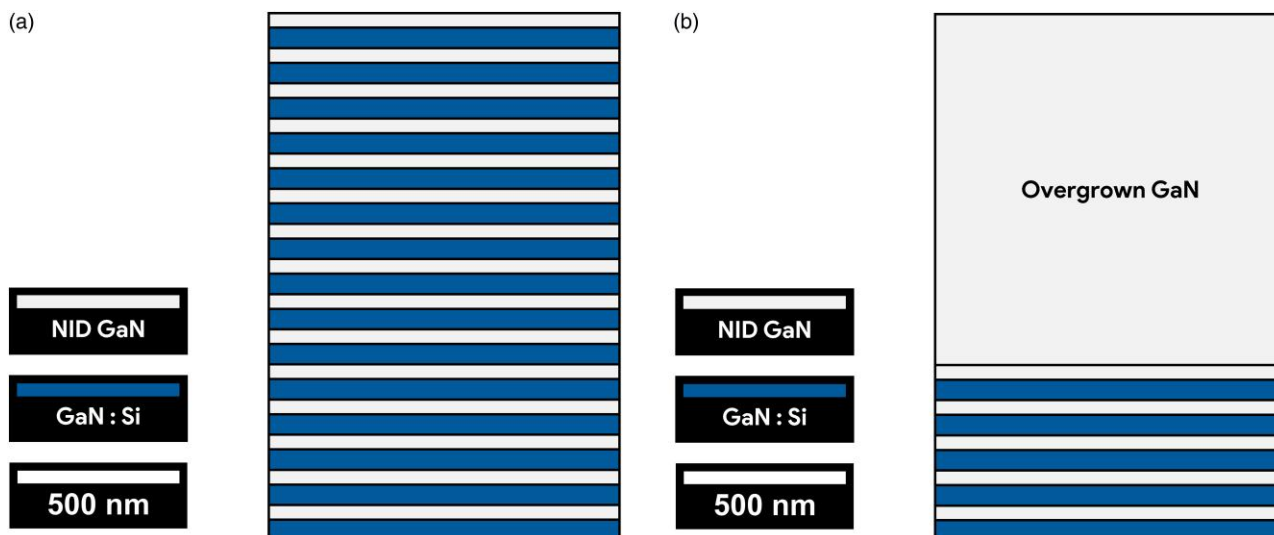


Fig. 1. As-grown and to-scale schematics of the investigated DBR periodic epilayers. Si-doped GaN layers are porosified after doping-selective ECE. **(a)** 15-Pair DBR and **(b)** 5-Pair DBR.

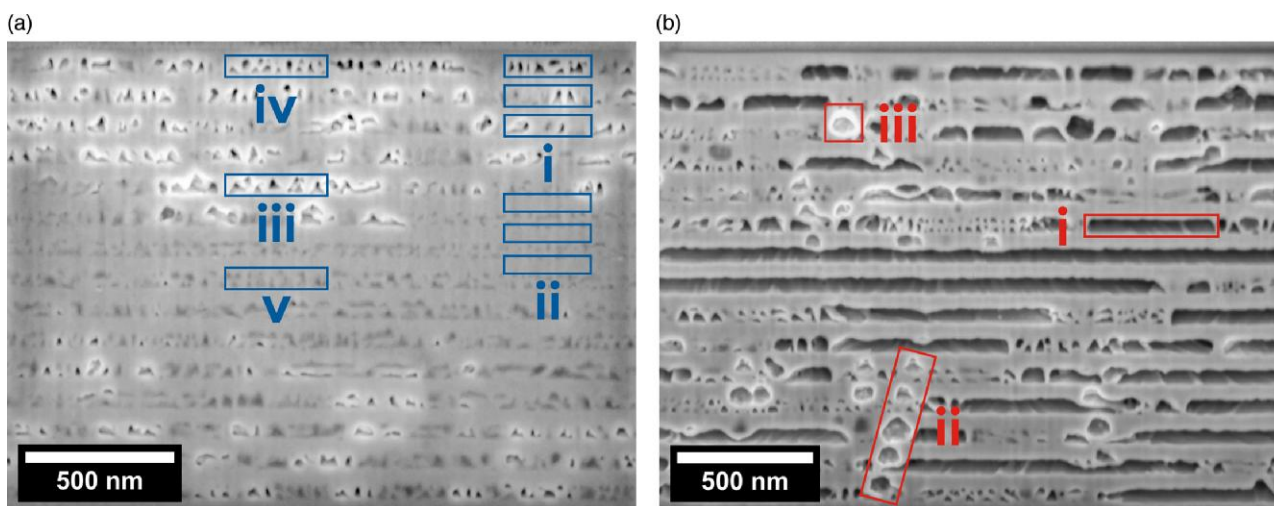


Fig. 2. Cross-sectional FIB-SEM of 15-pair porous GaN DBRs V_0 and $V_0 + 5 V$ using in-column SE imaging generated by a 2 keV LE. In addition to the periodic porosity, a topmost layer of protective Pt is seen. The image contrast is dominated by sectional topography but with additional contributions from charging and the pore-back effect. **(a)** V_0 and **(b)** $V_0 + 5 V$.

ScanAsyst tips from Bruker (Pittenger et al., 2010; Su et al., 2016).

Micrograph quantification was conducted in OriginPro V9.9.5 (OriginLab Corporation, Massachusetts, USA) and the Fiji distribution of ImageJ2 V1.54d (Schindelin et al., 2012). Monte Carlo beam-specimen interaction simulations were conducted in CASINO V2.5.1 (Drouin et al., 2007).

15-Pair Porous DBRs

Cross-sectional FIB-SEM

Cross-sectional imaging for both 15-pair porous GaN DBRs, V_0 and $V_0 + 5 V$, was obtained through FIB nanomachining followed by in-column SE-SEM at 2 keV LE, as shown in Figure 2. Such cross-sectional FIB-SEM uses an ion beam current of 1.5 nA to mill a trench, which is polished using a 50 pA ion beam.

These DBRs are etched through the top surface, so conserving this region is essential. To this end, the topmost layer above the NID GaN cap—most visible in Figure 2b—is a layer of protective Pt, which also reduces curtaining of the sample during sectioning (Cantoni & Holzer, 2014; Fager et al., 2020). Here, the use of electron beam Pt deposition avoids amorphization incurred from a faster Ga^+ assisted deposition (Kwong & Zhang, 2005).

V_0 is a mesoporous DBR similar to those widely studied in the literature and is presented in Figure 2a; image features i–v are highlighted. The ECE of Si-doped GaN has produced a periodic structure with alternating layers of porous GaN (Fig. 2a.i) and GaN (Fig. 2a.ii). Most observed pores appear fairly triangular (Fig. 2a.iii). Crucially, there is minimal encroachment of pores into NID GaN regions, as the cross-section appears congruent with the Figure 1a schematic. Lastly, within a single porous layer, several pores may be stacked vertically (Fig. 2a.iv).

Figure 2a also reveals some typical cross-sectional FIB-SEM aberrations. White highlights will often surround pore edges; these are not related to the section's topography but are more likely to be charging artifacts (Fig. 2a.iii) (Abe et al., 2009). There is potential for pore filling via sputtered atom redeposition (Giannuzzi & Stevie, 2010). Furthermore, preferential sputtering towards the bottom of pores may induce damage at these edges (Zhong et al., 2020). Finally, in the image center, the contrast between the pores and the GaN matrix is visibly diminished (Fig. 2a.v). This lack of contrast uniformity complicates the interpretation and quantification of porosity (Reimers et al., 2019).

Cross-sectional FIB-SEM of $V_0 + 5 V$ is depicted in Figure 2b; the FOV is closely matched to aid comparison. This DBR exhibits significantly increased porosity due to the higher applied electro-oxidation potential and is consistent with previous literature findings for etching at higher applied biases (Chen et al., 2012). Some of the nanoscale porosity seen for V_0 remains, but larger pores take up the majority of the material; specifically, micro-scale voids are observed—some of which extend outside of the $2.3 \mu\text{m}$ wide image (Mays, 2007) (Fig. 2b.i). Unlike V_0 , there is considerable porosity in nominally nonporous layers (Fig. 2b.ii). Charging artifacts are less common here but still observed (Fig. 2b.iii).

These cross-sections reveal no information about the nature of the porosity in the sample plane. The following *Plan-view BSE-SEM* section introduces our approach to using BSEs in the plan-view imaging of porous GaN DBRs.

Plan-view BSE-SEM

An image of a porous GaN DBR fabricated similarly to our V_0 DBR and captured using sequential milling and plan-view HAADF-STEM is shown in Figure 3. This DBR was previously studied by Massabuau et al. (2020b). By imaging in plan-view, the extended shape of the pores can be characterized as being branched, as outlined in Figure 3i, and they are also revealed to be radially aligned. Domains of branched porosity are observed, centered on black dots (Fig. 3.ii)—in a manner that is Voronoi-like (Jiang et al., 2011). Unetched GaN forms the borders between these partitions of porosity (Fig. 3.iii). In a purely cross-sectional workflow, accessing such in-plane

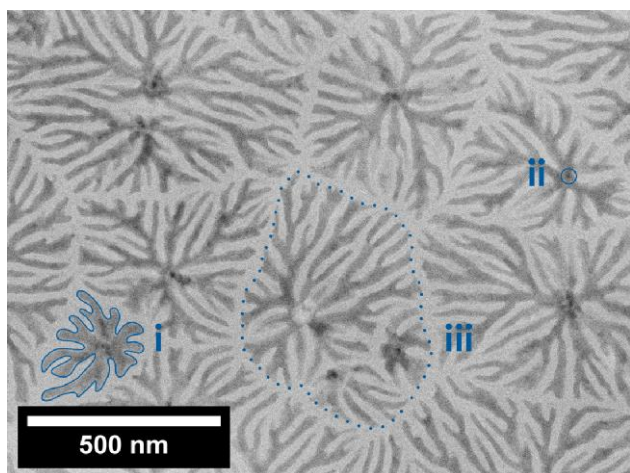


Fig. 3. Plan-view HAADF-STEM of a porous GaN DBR, determined to be comparable in porous morphology to the 15-pair porous GaN DBR V_0 ; here, image contrast is thickness-dependent.

information is difficult. In a further study applying this methodology for atomic resolution, Massabuau et al. (2020a) showed that for mesoporous DBRs akin to V_0 , the etchant accesses doped layers via nanopipes (Fig. 3.ii) that form at the cores of etched threading dislocations, which then act as vertical channels for the etchant and etch products.

As a proof-of-concept, plan-view sub-surface, BSE-SEM was conducted on the 15-pair porous GaN DBR V_0 , with a 20 keV LE. In Figure 4a.i, we observe nanoscale pores branched in a distinctly dendrite-like morphology (Wünsche et al., 2013). These branches radially emanate from central black dots as highlighted in Figure 4a.ii. Lastly, Figure 4a.iii features well-defined boundaries between discrete Voronoi-like porosity domains. BSE imaging intensity is typically defined by Z-contrast and, therefore, can be considered to be compositionally sensitive; however, the imaged samples consist solely of GaN with almost certainly no chemical species variation. Therefore, the contrast in Figure 4a can be described as being material density-contrast dominated. When comparing the BSE-SEM and HAADF-STEM modalities, we can identify high-density (white, GaN), medium-density (gray, sub-surface pores), and

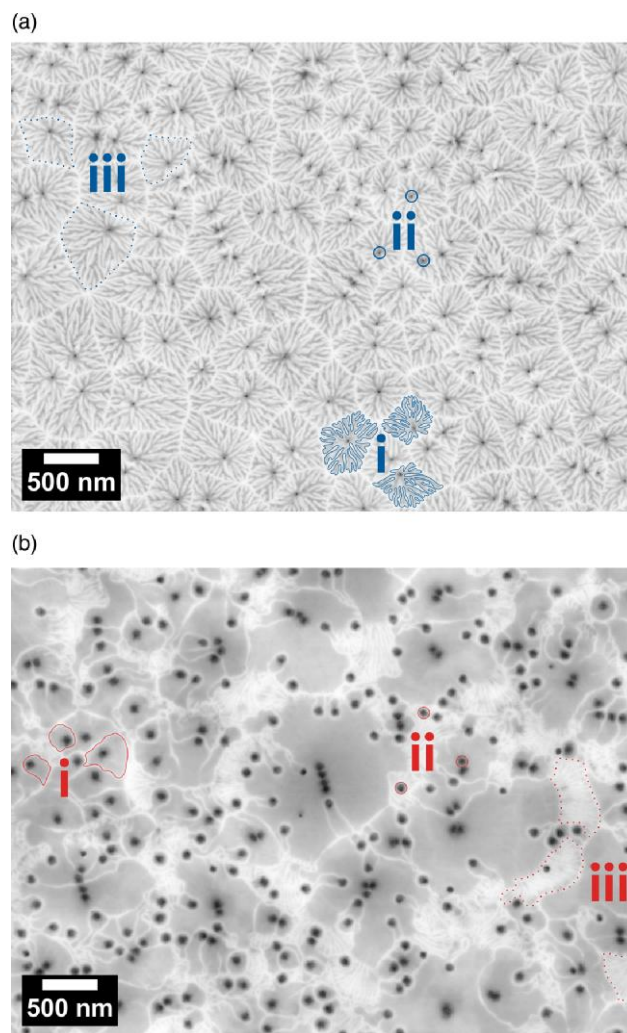


Fig. 4. Plan-view sub-surface BSE-SEM of 15-pair porous GaN DBRs V_0 and $V_0 + 5 V$. The micrographs are material density-contrast dominated: high-density (white, GaN), medium-density (gray, sub-surface pores), and low-density (black, open volumes at threading dislocation cores). (a) V_0 and (b) $V_0 + 5 V$.

low-density (black, open volumes at threading dislocation cores) regions.

Thus, the imaging conducted using plan-view BSE-SEM can reveal many of the same structural features as HAADF-STEM and can provide sufficient information to conclude that the HAADF-STEM imaged porous GaN DBR is broadly analogous to the observed porous morphology in the BSE-SEM of V_0 —captured non-destructively with only a fraction of the microscope capital cost.

Increasing the ECE voltage to $V_0 + 5$ V produces the morphology BSE-SEM imaged in Figure 4b. A dramatic loss of Voronoi-like domain structure and radially aligned branched porosity is seen. Through the outlines of Figure 4b.i, we can identify the micron-scale voids previously highlighted in Figure 2b by comparison of cross-sectional and plan-view microscopy. The circled black dots (Fig. 4b.ii) are often at the center of the etch fields, congruent with the known mechanism for defect-driven ECE. Furthermore, their density is within the threading dislocation density range for GaN on sapphire (ca. 1.1×10^9 cm⁻²) (Serafinćzuk et al., 2020). Lines of black dots, such as that centrally located in Figure 4b, correspond to the arrays of dislocations commonly seen in GaN on sapphire (Oliver et al., 2006). These black dots associated with etched threading dislocations have increased in diameter relative to V_0 and are discussed in more detail later through correlative microscopy. Finally, between the gray petals of the voids, the previously remarked nanoscale porosity is observed, with narrow, elongated pores (Fig. 4b.iii).

As seen in the Figure 1a schematic, the extent of the first porous layer is approximately 45 nm to 108 nm below the sample surface and likewise 153 nm to 216 nm for the second porous layer. In both 15-pair porous DBRs, at a minimum, the uppermost NID GaN cap (ca. 45 nm) is being imaged through to access information from the first porous layer. Therefore, the maximum cap thickness through which such information can be probed and the extent to which there is multi-porous layer convolution are now critical investigation points.

These results demonstrate that BSE-SEM may be valuable to the efficient characterization of pore morphologies in studies assessing the impact of changing etch conditions. Indeed, the differences between etching at two different voltages are evident in the datasets presented so far. Next, further examination of $V_0 + 5$ V through the impact of the SEM LE and comparison to other microscopy techniques will aid an interpretation of the observed contrast.

Correlative Microscopy

Next, we use a correlative microscopy approach (Ando et al., 2018) (also known as multi-microscopy O'Hanlon et al., 2020) for a comparison between the BSE imaging methodology introduced above and three standard techniques, thus identifying the unique structural information or image characteristics attainable using BSE-SEM. Datasets in the same ROI were initially captured using non-destructive PeakForce Tapping AFM and SEM using in-column SE and annular BSE detectors. Afterwards, tomographic FIB-SEM was conducted there using an in-column SE detector. Together, these techniques allow for comparing surface, near-surface, and sub-surface imaging. The images are shown in Figure 5 and presented in the order captured.

The DBR etched at $V_0 + 5$ V was used for these investigations because the DBR etched at V_0 is dominated by nanopores, presenting a spatial resolution challenge for

tomography. Furthermore, etching at V_0 leaves the sample's surface almost unaltered relative to the as-grown sample (Zhu et al., 2017). The surface is subsequently very smooth, which makes identifying the same ROI across multiple microscopes difficult. The DBR etched at $V_0 + 5$ V, on the other hand, has larger pores (as has been established through the prior cross-sectional and plan-view imaging) and also (as will be shown below) has surface features which have arisen as a consequence of etching, which allow easier ROI identification.

Starting with the surface topographic data in the PeakForce Tapping AFM image: the vertically orientated stripes running through Figure 5a are the atomic steps that result from step-flow growth in MOVPE of GaN and which are frequently seen in the AFM of unetched GaN (Jarman et al., 2019). Numerous black pits are seen, which we interpret as arising at threading dislocations (Massabuau et al., 2020a). As a consequence, the pit density is ca. 1.2×10^9 cm⁻², which is consistent with the number density of dislocations expected in such GaN/sapphire samples (Oliver et al., 2006). Moreover, an array of small pits is observed at the image's center, a formation typical of dislocation arrays in GaN (Oliver et al., 2006). Lastly, the interpretation of these pits as dislocation-related is consistent with our interpretation of black dots in this DBR's Figure 4b BSE image as dislocation channels. These pits are (43 ± 1) nm in width and (26 ± 1) nm in depth, whereas, for unetched GaN, these values would typically be around 20 nm and less than 1 nm, respectively (Oliver et al., 2006). Hence, the pits have enlarged upon etching, proving that ECE has occurred. However, no other evidence of porosity is observed. Plasma cleaning was conducted before imaging, yet debris remains visible on the surface.

Next, we consider the 2 keV LE SE-SEM image of Figure 5b. Here, dislocation-related pits are once more visible, but the atomic terraces are no longer resolved. However, the observed contrast offers no additional information about sub-surface porosity relative to AFM. Hence, it appears only to contain information from the topmost 45 nm of NID GaN. The central array of pits was repeatedly used for microscope adjustment before image capture. The resulting carbonaceous contamination is only visible in this SEM configuration. This marker was later used to identify this ROI for tomographic FIB-SEM. Almost all visible pits are encircled by a bright ring not previously seen in AFM. Whether the rings are a charging artifact or relate to edge effects is unclear (Cizmar et al., 2008).

The ratio of SE_1 (generated by the incident beam) to SE_2 (generated by BSEs), from a 2 keV LE beam-specimen interaction, is expected to be dominated by the former (Cazaux, 2012). Additionally, SE_1 s are known to conserve both the lateral extent of primary electrons within the focused probe as well as the SE shallow sampling depth, as governed by their rapidly decaying escape probability (Goldstein et al., 2017). Consequently, and also when considering the observed similarities in near-surface information between AFM and 2 keV SE-SEM in Figure 5, these data suggest that SE_1 dominate the contrast observed in the latter (Kumagai & Sekiguchi, 2009).

The 20 keV LE SEM in Figures 5c and 5d was captured simultaneously using both SE and BSE signal types. The SE-SEM in Figure 5c now reveals contrast, which we can identify by comparison to the earlier Figure 4 BSE-SEM as being related to porosity. The central pit cluster observed in Figures 5a and 5b appear similar. A gray flower-like area surrounds the cluster, which we interpret as a micro-scale void, as seen in the prior cross-sectional FIB-SEM of Figure 2b. Consequently, at high LE, even in

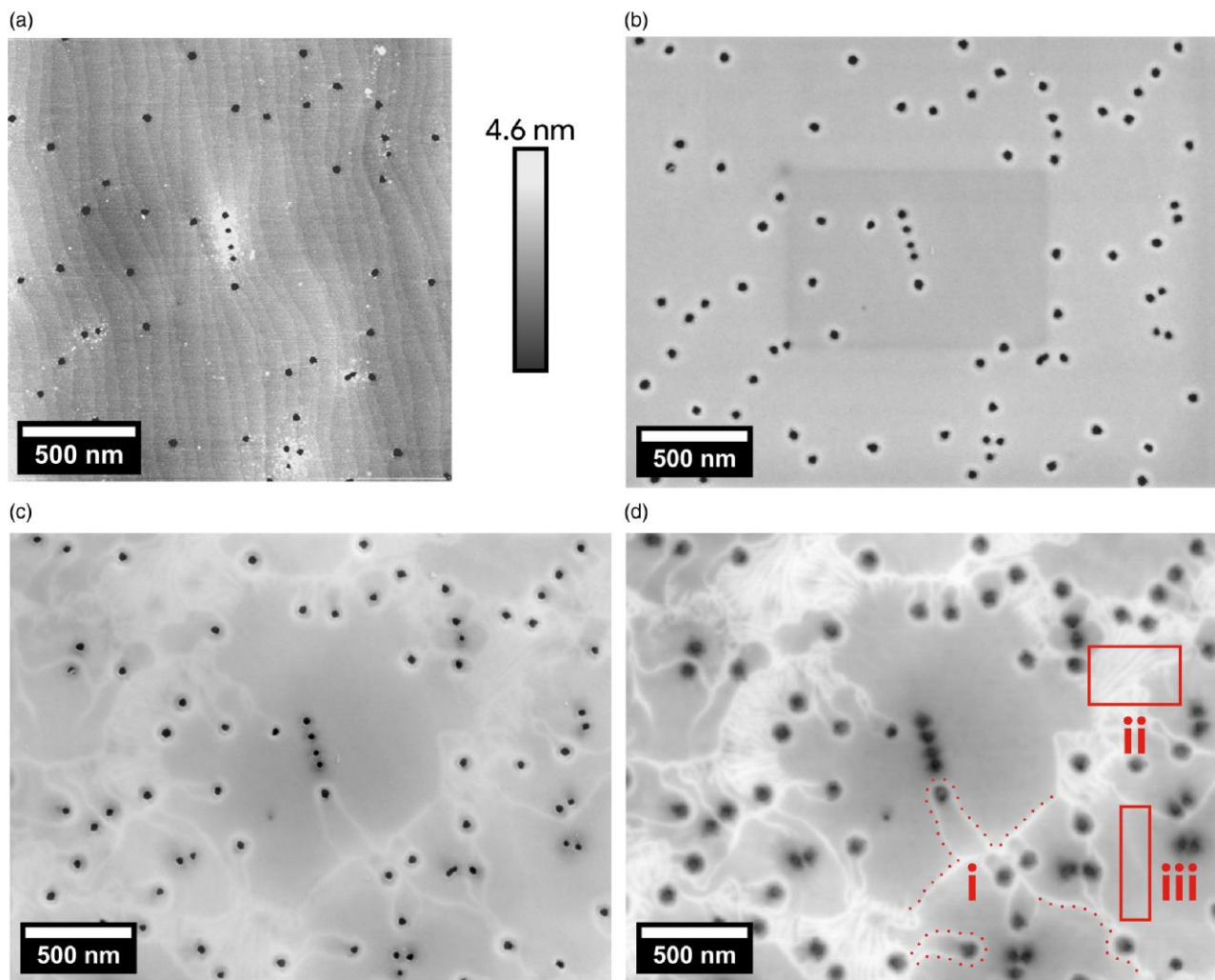


Fig. 5. Multi-microscopy captured in the same ROI of 15-pair porous GaN DBR $V_0 + 5 V$, imaged using PeakForce Tapping AFM (a), SE-SEM using the in-column SE detector at LEs of 2 keV (b) and 20 keV (c), and BSE-SEM at 20 keV LE using the annular BSE detector (d).

SE-SEM, the spatial resolution and image contrast present are at least sufficient to distinguish between large pores, regions of fine-branched porosity, and channels associated with threading dislocations. On the other hand, the image contrast associated with the different porous morphologies in the sub-surface structure appears superior in the BSE-SEM image. The dislocation-related features, which appeared broadly similar in Figures 5a–5c, now appear to have larger diameters. Both 20 keV LE images show significantly less contrast related to surface contamination.

SE₂s have a dependency on the local BSE yield generating them and, therefore, inherit BSE lateral distribution and depth information characteristics (Goldstein et al., 2017). Consequently, the SE₂ signal would be expected to possess similar morphological information (Cazaux, 2012). At 20 keV LE, the overall similarity between SE-SEM and BSE-SEM in Figure 5 suggests that SE₂s dominate the contrast observed in the former.

Tomographic FIB-SEM

Finally, a FIB-SEM tomograph was captured using conventional serial block face imaging, in the same ROI as Figure 5 (Cantoni & Holzer, 2014; Griffin et al., 2020). Voxel dimensions are approximately $(4 \times 4 \times 10)$ nm; the FOV is ca. $2.3 \mu\text{m} \times 1.8 \mu\text{m}$.

The 10 nm slice thickness facilitates the capture of a larger tomograph but introduces a resolution anisotropy. The first four porous layers of $V_0 + 5 V$ have been virtually reconstructed in plan-view and are shown in Figure 6; however, there are horizontal distortion bands due to data collection instability. Our intention is to reconstruct the central field of porosity that can be seen across all four reconstructions. Videos of the tomograph are shown in the Supplementary Material (S1 and S2).

Given the similarities between Figure 3 (showing a single layer of porous GaN in STEM) and the BSE-SEM of V_0 in Figure 4a, it is tempting to assume that the BSE image is dominated by the first porous layer, 45–108 nm sub-surface. However, it is essential to confirm this as a convolution of several porous layers will complicate interpretation and limit the accuracy of quantitative measurements. To this end, the tomograph can identify which regions of unetched GaN contribute to BSE-SEM intensity and from which layer.

The reconstruction of the first porous layer in Figure 6a suggests that the SEM contrast seen in Figures 5c and 5d is dominated by the morphology here. An example is annotated in Figures 5d.i and 6a.i, relating to the bottom of the large gray flower-like area surrounding the central cluster of pits. We observe the well-defined interface between the micron-scale void and the unetched GaN. Likewise, a region of branched

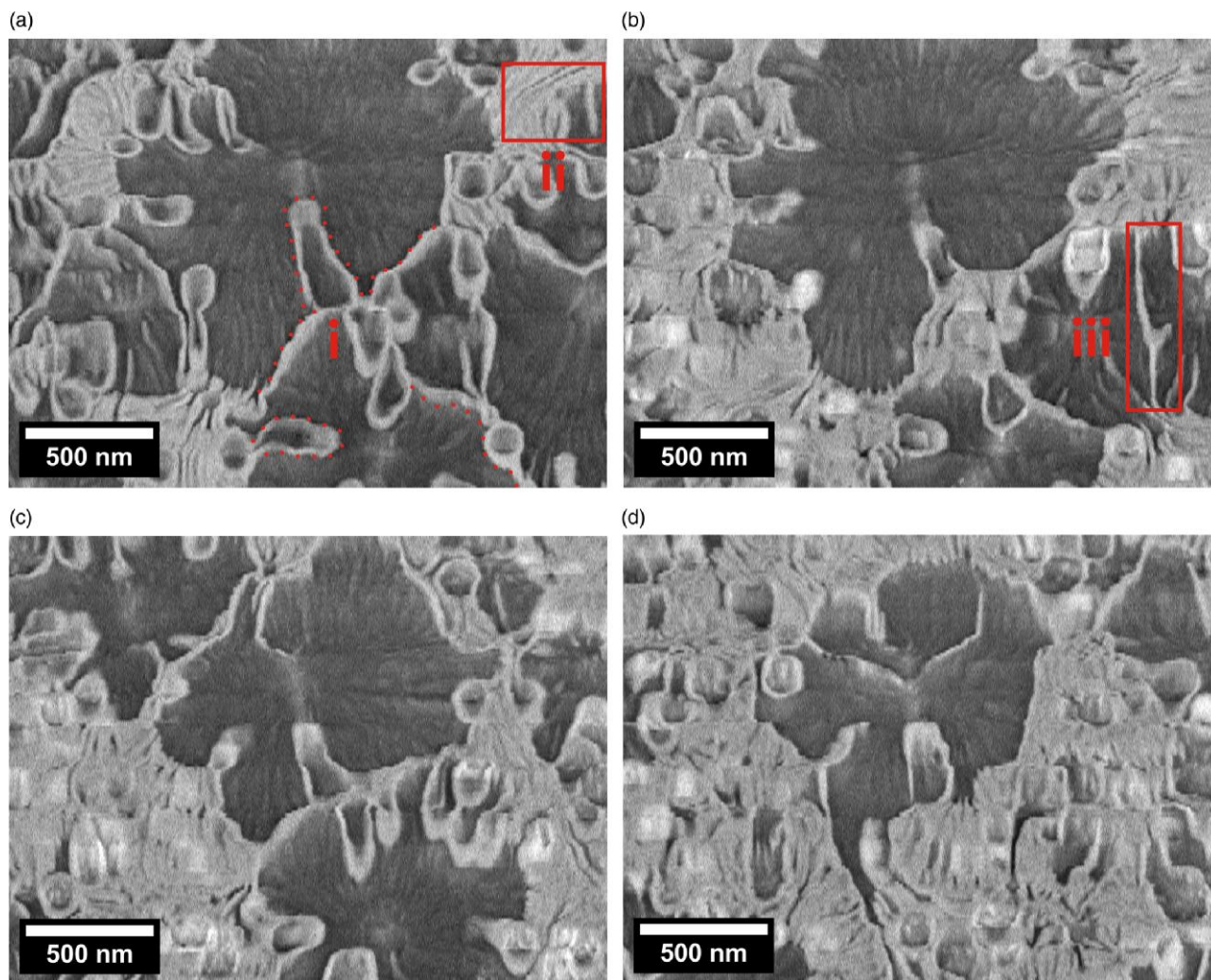


Fig. 6. Reconstructed plan-views of 15-pair porous DBR $V_0 + 5$ V, as derived from tomographic FIB-SEM; dataset is captured in the same ROI as [Figure 5](#) for correlative microscopy. Voxel dimensions are approximately $4 \times 4 \times 10$ nm with cubic interpolation between slices; the field of view is ca. $2.3 \mu\text{m} \times 1.8 \mu\text{m}$. (a) First porous layer, (b) second porous layer, (c) third porous layer, and (d) fourth porous layer.

nanopores is highlighted in both [Figures 5d.ii](#) and [6a.ii](#) and can also be directly correlated between the two images. Consequently, features observed in BSE-SEM that are resolved with a high contrast or spatial resolution are also seen in the tomographic reconstruction of this layer. Very few features, if any, in the BSE image are absent from this reconstruction.

The reconstruction of the second porous layer is shown in [Figure 6b.iii](#). It reveals a vertical strip of unetched GaN directly beneath a large void in the first porous layer. This strip of GaN can also be seen in [Figure 5d.iii](#) but appears blurry with low contrast. Identifying structural details in the BSE image, such as the protrusion nearly halfway down the strip, is impossible. [Figures 6c](#) and [6d](#) depict the third and fourth porous layers, respectively. However, we have not identified features in these reconstructions that can be directly correlated to BSE-SEM.

The virtual camera can also reconstruct the sub-surface morphology of the black pits. The transition through the first ca. 45 nm of NID GaN can be described as a gradual increase in diameter, as shown in [Figure 7](#); they then vanish in the first reconstructed porous layer in [Figure 6a](#). Only to reappear in the next NID GaN layer, open with depth, and then vanish in the second reconstructed porous layer in [Figure 6b](#). This oscillation repeats throughout the DBR. Therefore, the increased pit

diameter when comparing 20 keV BSE-SEM to 20 keV SE-SEM reflects the former containing more information about the evolution of pit morphology through the first NID GaN layer.

These correlative microscopy results show that in our 20 keV LE BSE-SEM approach, images of the porous GaN DBR etched at $V_0 + 5$ V are dominated by the features in the first porous layer with low contrast and highly diffuse contributions from the second layer.

Primary Electron Landing Energy

This section addresses the optimized BSE-SEM parameters for imaging sub-surface porosity in these DBRs. We will identify the optimal signal type and primary electron landing energy by experimental quantification of image contrast and spatial resolution.

In [Figure 8](#), we display split images captured simultaneously using BSE (left) and SE (right) signal types in the same ROI. Additional microscope parameters are held constant, which include: 3.5 mm working distance, $30 \mu\text{m}$ aperture size, 50 ns pixel dwell time, and 0.7 nm raster scan pixel size. The two lattermost parameters combine for a ca. 11 minute scan time across $(1.4 \times 2.1) \mu\text{m}$. Each dual-signal image should

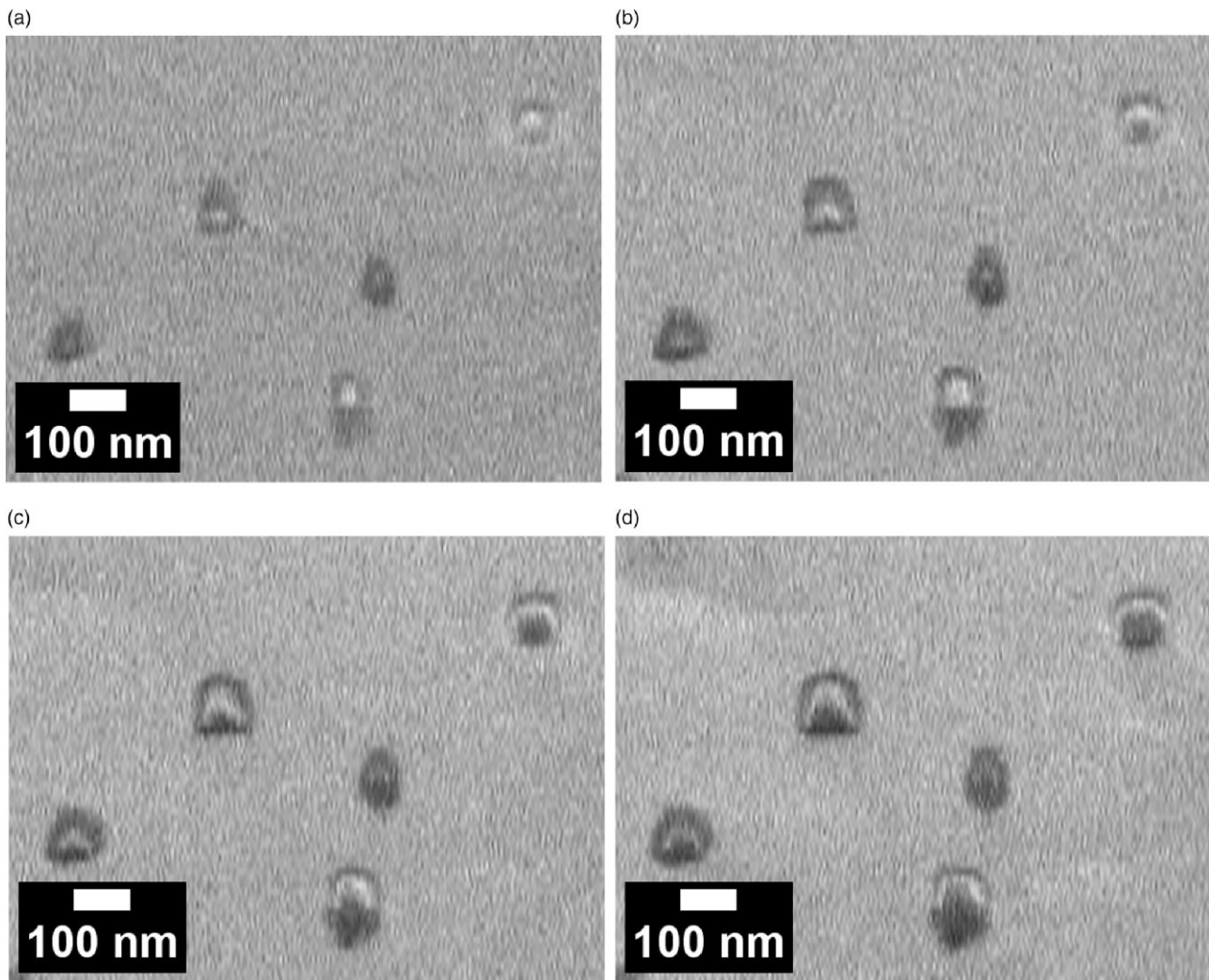


Fig. 7. Reconstructed plan-views of 15-pair porous DBR $V_0 + 5 V$, as derived from tomographic FIB-SEM. Virtual images show the sub-surface evolution of etched black pits associated with threading dislocations in the topmost ca. 45 nm of GaN. (a) 20 nm sub-surface, (b) 25 nm sub-surface, (c) 30 nm sub-surface, and (d) 35 nm sub-surface.

predominantly differ by LE, with images for 10 keV, 15 keV, 20 keV, and 25 keV displayed in Figures 8a–8d, respectively. Using a Faraday cup, measured probe currents are around 180 pA, 230 pA, 280 pA, and 250 pA, respectively.

Initial inspection shows that BSE-SEM reveals more of the nanoscale branched porosity that permeates the white regions of minimally etched GaN as the LE increases. This impression is most apparent when considering Figures 8a and 8b, as moving from a LE of 10 keV to 15 keV provides what appears to be the most discernible improvement in image contrast. Furthermore, when examining 20 keV and 25 keV LEs, as shown in Figures 8c and 8d, a further increase in image contrast over 15 keV is observed. However, distinguishing between 20 keV and 25 keV now necessitates a quantitative approach.

Next, let us consider SE-SEM. Firstly, the image contrast produced with a 10 keV LE (Fig. 8a) appears more substantial than that produced in BSE-SEM. Also, the image contrast appears to deteriorate as the LE increases to 15 keV (Fig. 8b) and 20 keV (Fig. 8c). Finally, a near-total loss of image contrast was observed at 25 keV (Fig. 8d).

For LEs ≤ 20 keV, the Zeiss GeminiSEM 300 uses an additional in-column accelerating potential (between the ‘beam

booster’ and polepiece) (Jaksch & Martin, 1995; Zhang et al., 2023). This behavior improves spatial resolution and attracts and accelerates generated SEs back up the column towards the in-column SE detector (Tandokoro et al., 2018). However, the beam booster is switched off at higher LE values, significantly reducing the in-column SE signal collected. Our subsequent quantification of SE-SEM is necessarily limited to 10 keV, 15 keV, and 20 keV LEs.

Quantification—Image Contrast

The principle information sought through BSE-SEM is the contrast between porous and non-porous regions, with sufficient spatial resolution to resolve nanostructure. The following equation defines the contrast-to-noise ratio (CNR). This measure omits normalization to a background signal, allowing quantification using solely the information provided in single micrographs:

$$\text{CNR} = \frac{\text{Contrast}}{\text{Noise}} = \frac{|\mu_1 - \mu_2|}{\sqrt{\sigma_1^2 + \sigma_2^2}}. \quad (1)$$

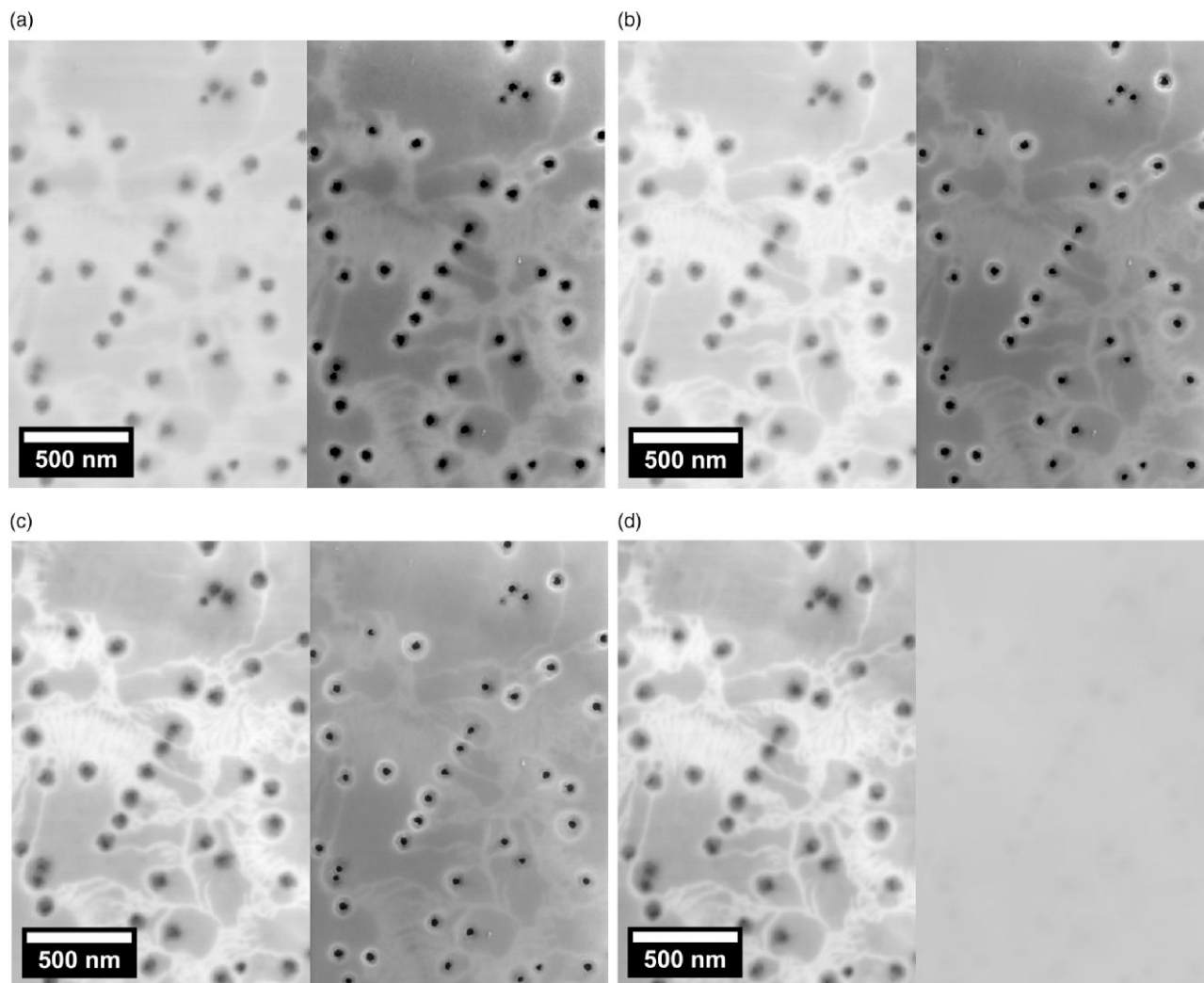


Fig. 8. BSE-SEM and SE-SEM as a function of LE, in the same ROI of 15-pair porous DBR $V_0 + 5$ V. LE values range between 10 keV and 25 keV. The BSE signal appears on the left side of each image, with the SE signal on the right side. (a) 10 keV, (b) 15 keV, (c) 20 keV, and (d) 25 keV.

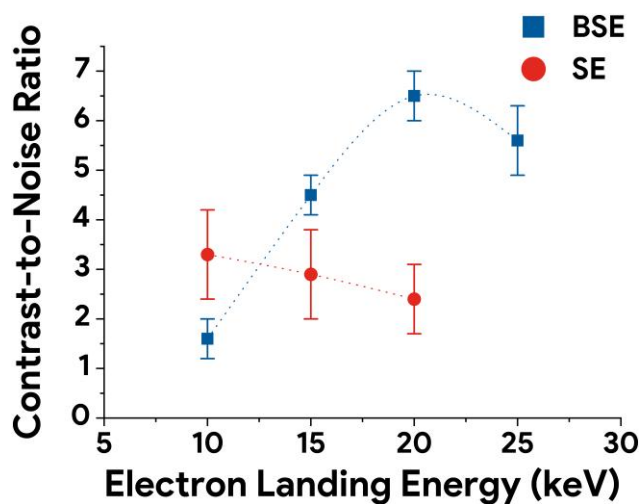


Fig. 9. CNR as a function of LE and signal type. Higher CNR values are correlated with improved image quality. Dotted splines are drawn exclusively to guide the eye.

In general, $\mu_1, \mu_2, \sigma_1, \sigma_2$ here are the respective expectation values and standard deviations of two different signals contained within a single micrograph (Welvaert & Rosseel, 2013; Timischl, 2014; Bergin et al., 2019). Here, we consider the signal within the pores, μ_1 , and compare it to the signal from unetched GaN, μ_2 , when considering the noise in each, σ_1 and σ_2 , respectively (Jönsson & Björk, 2020).

To estimate CNR, local samples of 1,000 pixels were captured in gray porous image regions and white non-porous regions. Each sample is associated with a mean intensity, μ , and corresponding standard deviation, taken as a measure of the noise, σ , as described in equation 1. To characterize the porous signal within an image, μ_1 , through a singular expectation value, six samples are averaged; the process is repeated for the non-porous signal, μ_2 (Heo et al., 2022). CNR is plotted for each signal type and LE configuration in Figure 9.

A statistically significant CNR improvement with increasing LE is observed for BSE-SEM, peaking at 20 keV with a CNR of 6.5 ± 0.5 . A slight decrease from this value occurs at 25 keV. The larger interaction volume here may yield more signal

from the second porous layer and contribute additional noise. This evolution in CNR is more significant than expected based solely on the measured increase in probe current. However, SE-SEM has a CNR that is almost invariant or perhaps decaying with LE. The highest CNR occurs at 10 keV with a 3.3 ± 0.9 value. The relative contrast illustrates that the SE signal provided a superior CNR at 10 keV, fell behind the BSE signal at 15 keV and fell further behind at 20 keV. By this point, the BSE CNR is nearly three times greater than the SE CNR.

Quantification—Spatial Resolution

Next, we develop a metric for the change in spatial resolution with SEM configuration. Throughout this LE dataset, it is possible to observe filaments of unetched GaN with nanoscale width. Line profiles can be extracted at these locations, where the peak intensity corresponds to a white GaN filament against a gray porous background. These peaks can be fitted with a Gaussian function, and an associated full width at half maximum (FWHM) can be extracted.

These results are plotted in Figure 10, where a reduction in FWHM implies improving spatial resolution. For BSE-SEM, a statistically significant spatial resolution improvement with increasing LE is observed, with an optimum observed at 20 keV with an FWHM of (25 ± 1) nm. Mirroring the CNR analysis, the spatial resolution worsens at 25 keV. For SE-SEM, a statistically significant spatial resolution improvement with increasing LE is also seen, with the best value achieved at 20 keV with an FWHM of (32 ± 1) nm. These results illustrate that both signal types produce images that sharpen with LE. Moreover, and essentially matching the trends established through CNR quantification, not only does the BSE signal produce a sharper image of the sub-surface structures at each LE, but the improvement over SE imaging also increases with LE.

In summary, these data suggest that the optimum combination of LE and signal type when pursuing maximal image contrast and spatial resolution of sub-surface porosity in this $V_0 + 5$ V DBR is an SEM operating at or near a 20 keV LE and BSE imaging. The rationale for these observations will be discussed in Discussion section.

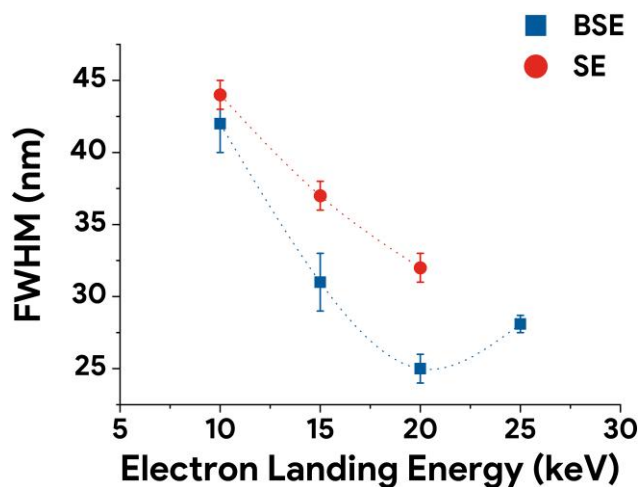


Fig. 10. Spatial resolution quantification: GaN filament intensity profile FWHM as a function of LE and signal type. Lower values are correlated with improved image quality. Dotted splines have been drawn exclusively to guide the eye.

5-Pair Porous DBR

Next, we address the depth below the surface at which obtaining an image with meaningful spatial resolution and image contrast is still possible. This notion may be described as assessing the “information depth”. In the literature, information depth has been used to address to what depth a buried object within a host matrix can be resolved or down to what depth an interface between two materials can be distinguished (Rau & Reimer, 2001; Goldstein et al., 2017). With spatial resolution and image contrast quantified for the BSE-SEM of porous DBR morphology, our final experimental investigation addresses the maximal achievable information depth (Piños et al., 2017).

The 5-Pair, porous GaN DBR with ca. 1,000 nm GaN overgrowth investigated here is schematically illustrated in Figure 1b and imaged via cross-sectional FIB-SEM, as depicted in Figure 11. Five porous layers are observed, as well as the overgrown GaN. Uniformity is poor, with the fourth and fifth layers seemingly less porosified than those above. Furthermore, many pores intrude into nominally NID GaN regions.

FIB nanomachining was used to mill four trenches of reduced GaN cap thicknesses into the as-etched surface. This approach allowed the same porous layers to be imaged through different cap thicknesses. As this was conducted in a top-down perspective whereby the ion beam is perpendicular to the sample surface, there will be considerable implantation, amorphization, and redeposition, which will contribute to altering the newly exposed material, particularly as this was performed with a 30 kV Ga⁺ ion beam (Volkert & Minor, 2007).

Surface, Near-surface, and Sub-surface Microscopy

Once more, AFM, BSE-SEM, and tomographic FIB-SEM were applied in concert. Figure 12 shows a PeakForce Tapping AFM image of the region in which the GaN cap thickness has been reduced by FIB milling. Four rectangles are observed, with the bright white area between them denoting the as-overgrown (unmilled) surface. Each rectangle is a milled area, with the black region relating to the deepest milling or thinnest cap. By measuring the depths of these trenches in AFM, we calculate that the GaN cap thickness progresses

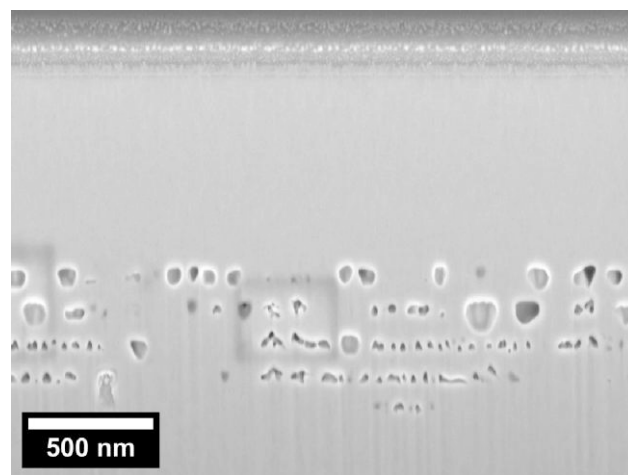


Fig. 11. Cross-sectional FIB-SEM of the 5-Pair, porous GaN DBR with ca. 1,000 nm GaN overgrowth. In addition to the periodic porosity, a topmost layer of protective Pt is seen. The image contrast is dominated by sectional topography but with additional contributions from charging and the pore-back effect.

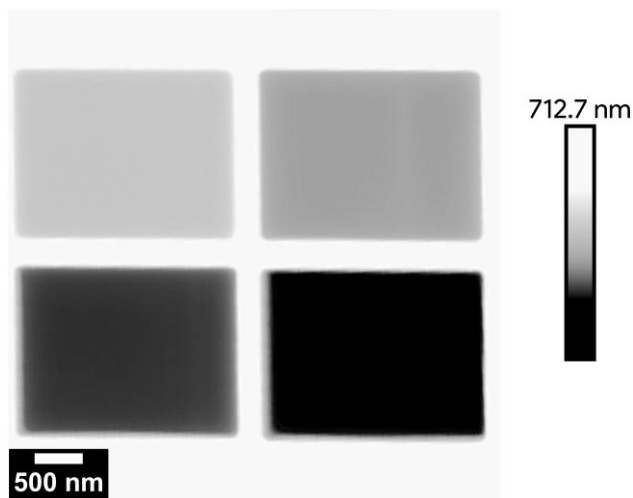


Fig. 12. PeakForce Tapping AFM, imaging of a quartet of GaN cap thicknesses FIB nanomachined into the 5-Pair, porous GaN DBR with ca. 1,000 nm GaN overgrowth. From bright to dark, the contrast progression of GaN cap thickness is 474 nm, 383 nm, 295 nm, and 190 nm, respectively. The white area denotes the as-overgrown surface.

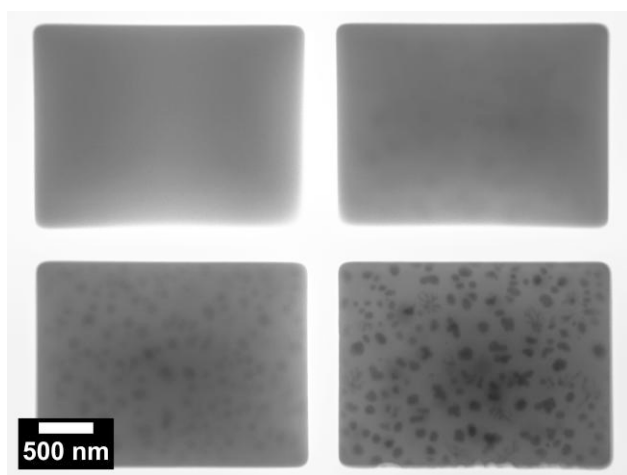


Fig. 13. Plan-view sub-surface BSE-SEM of the 5-Pair, porous DBR with ca. 1,000 nm GaN overgrowth, with a FIB nanomachined quartet of GaN cap thicknesses. The left-to-right GaN cap depth progression is 474 nm, 383 nm, 295 nm, and 190 nm, respectively.

from approximately 474 nm to 383 nm to 295 nm and to 190 nm, as the trenches get deeper. As can be seen from the uniform shade across the bottom of each trench, the nanomachining process has achieved a uniform depth and a flat bottom to the trenches. No significant variations in trench depth are observed, which would be sufficient to compromise later BSE-SEM interpretation.

Figure 13 shows the rectangles of different GaN cap thicknesses imaged through the previously optimized 20 keV LE BSE-SEM methodology. BSE imaging in the top-left rectangle, with the thickest GaN cap (ca. 474 nm), yields no nanoscale contrast variations. Still, it does produce the expected reduction in intensity relative to the as-etched surface. Imaging through ca. 383 nm of GaN (top-right) yields a similar result, with minimal nanoscale contrast but a further reduction in intensity. Nanostructure, which we attribute to porosity, is first observed at a ca. 295 nm cap thickness (bottom-left); the

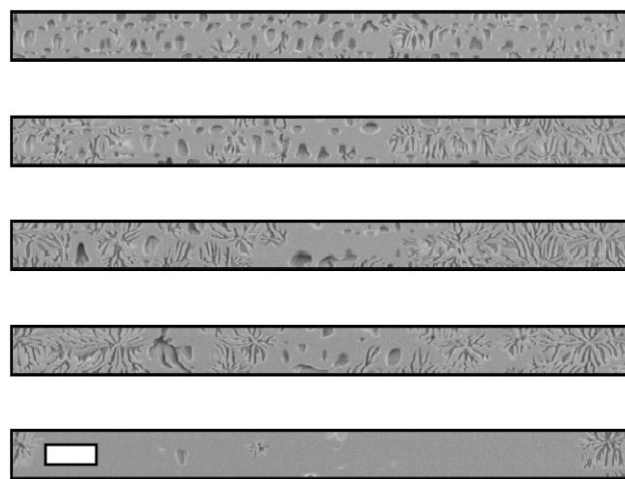


Fig. 14. Reconstructed plan-views of the 5-pair, porous GaN DBR with ca. 1,000 nm GaN overgrowth, as derived from tomographic FIB-SEM. Voxel dimensions are approximately $(2 \times 2 \times 10)$ nm with cubic interpolation between slices. The scale bar represents a width of 500 nm.

contrast is poor, and image features are diffuse. Lastly, inspecting the rectangle with a cap thickness of ca. 190 nm (bottom-right) reveals a less blurry nanostructure with greater contrast.

To check that the nanostructure observed with BSE-SEM is consistent with the pore structure in the first porous layer, tomographic FIB-SEM was performed in a different ROI. Depicted in Figure 14 are the five porous layers as reconstructed plan-views. A distortion band is seen near the top of each image due to microscope instability. Consistent with the cross-sectional FIB-SEM in Figure 11, a lack of layer-to-layer uniformity is observed in the tomograph, particularly in the fifth layer. The pores in the topmost porous layer have a spherical-like structure with little branching. The typical spherical diameter occupies a range of about 50 nm to 150 nm. The branch widths occupy a range of about 20 nm to 40 nm. Both are consistent with the morphology observed in the deepest milled rectangle using BSE-SEM. Branched porosity is seen in the second, third, and fourth layers, more akin to the mesoporous DBRs imaged in Figures 3 and 4a. Here, the critical point is that with the 190 nm cap, 20 keV LE BSE-SEM can image the porosity in the uppermost porous layer, and there appears to be minimal influence from the layers further down, consistent with our earlier results.

Monte-Carlo Simulations

Beam-specimen interactions were simulated using CASINO to further elucidate BSE-SEM information depth (Drouin et al., 2007). Such simulations are a function of the AFM-derived cap thicknesses approximated to be 474 nm, 383 nm, 295 nm, and 190 nm, above the 5-pair porous DBR shown in Figure 1b. Also, the four cap values include the 45 nm of NID GaN between the $1 \mu\text{m}$ of overgrown GaN and the first 63 nm of porous GaN.

The porosity was estimated from additional cross-sectional FIB-SEM and set to a constant 30% for each porous layer. The simulated porosity was approximated as a change in GaN density, which is set at 6.15 g/cm^3 and then periodically reduced to 4.305 g/cm^3 . This approach ignores the unintended

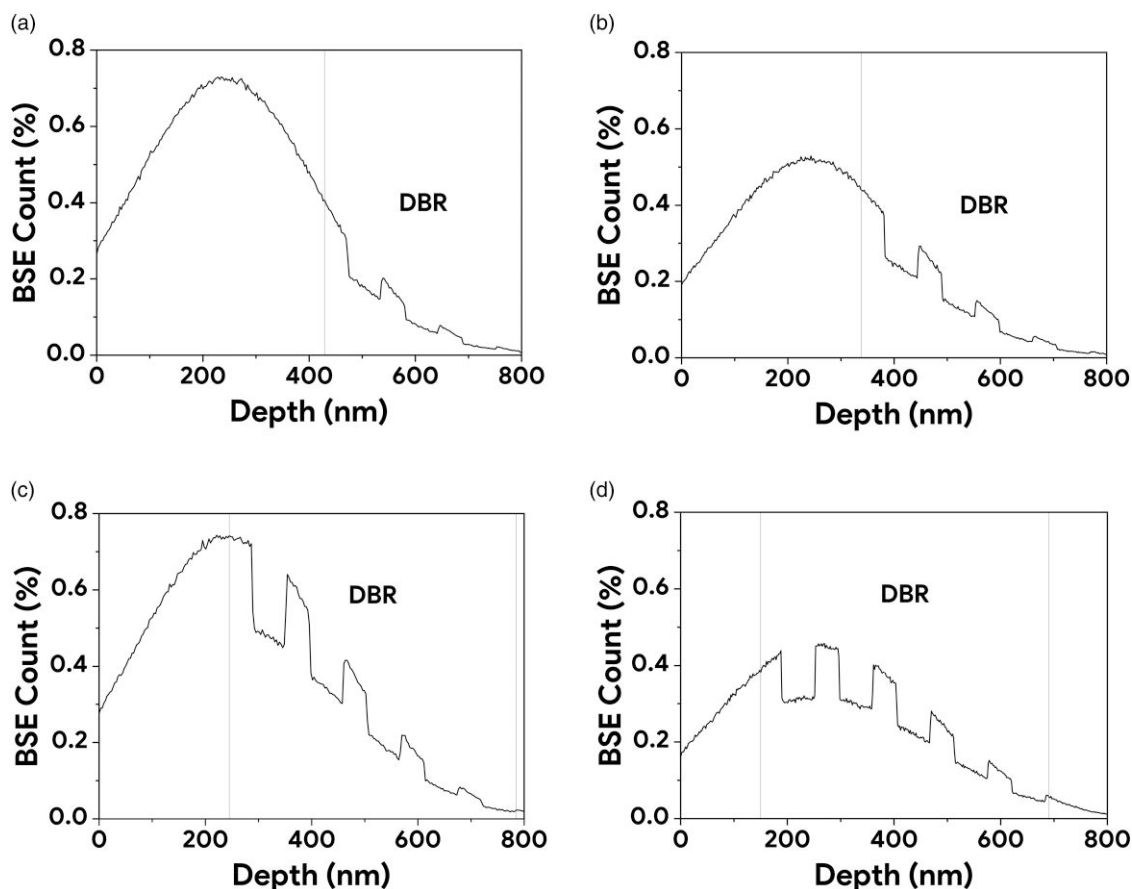


Fig. 15. CASINO simulations of BSEs as emitted from the 5-Pair porous GaN DBR with 30% porosity. Simulated variable cap thicknesses are derived from AFM. Plotted normalized histograms are the z-depth of emitted BSEs inside the sample. Graph arrangement matches the associated BSE-SEM. The three regions of interest are the (variable) GaN cap, porous GaN DBR, and GaN buffer. (a) 474 nm cap, (b) 383 nm cap, (c) 295 nm cap, and (d) 190 nm cap.

porosification of the NID layers and the specific pore morphology. For each configuration, 10 million incident primary electrons were simulated, with 20 keV LE and 10 nm beam radius.

The plotted normalized histograms depicted in Figure 15 show the depth from which BSEs arise and are expressed as a percentage of the total BSE count. The arrangement of the four graphs matches the corresponding imaging data in Figure 13. The three areas of interest are the (variable) GaN cap, porous GaN DBR, and the GaN buffer below. A key discussion parameter will be the peak position and its relation to the first porous layer.

Figure 15a shows the BSE count as a function of depth within the sample for the DBR region with a 474 nm cap; a line denotes the interface between the overgrown GaN cap and the start of the porous DBR structure. Most of the BSEs here appear to originate from the cap with the peak value at a depth of ca. 240 nm. The three count dips relate to the first three porous layers.

Figure 15b shows the 383 nm GaN cap simulation. Here, the porous layers still do not intersect the peak position, which appears at a depth of ca. 233 nm, with the bulk of the BSE counts originating from the non-porous cap. Figure 15c shows the simulation of the 295 nm cap structure for which some signature of nanostructure was seen in BSE-SEM. Here, the peak position lies at a depth of ca. 220 nm, and the first porous layer is starting to overlap with that peak.

Finally, Figure 15d shows the simulation of the 190 nm cap structure corresponding to where porosity was resolved most clearly. Here, not only is the first porous layer overlapping with the peak of the curve (at 240 nm,) but a comparison with Figure 15c suggests that one might now expect contrast from at least one additional porous layer, which may explain the appearance of additional blurred features in addition to those that are well-resolved. These results are consistent with the correlative tomographic FIB-SEM of 15-pair porous DBR $V_0 + 5$ V (Fig. 6), where we identified faint signatures of the second porous layer observed in sub-surface BSE-SEM (Fig. 5).

Discussion

To tie together the various sub-surface imaging experiments explored here, we will consider what expectations of image contrast, spatial resolution, and information depth can be derived from commonly used empirical or semi-empirical expressions—whilst also drawing comparisons with BSE-SEM studies from the broader literature.

Image Contrast

Rau & Reimer (2001) considered the contrast between Au and Cu sub-surface regions embedded within an Al host material. They investigated image contrast as a function of LE and the embedded depth. Equation 2 is a longitudinal range

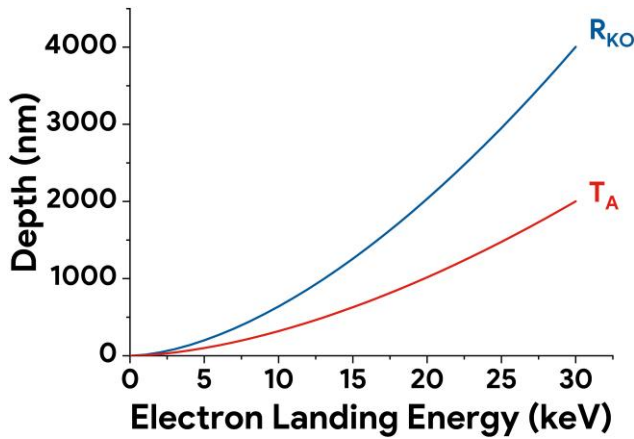


Fig. 16. The longitudinal extent of the normalized electron range, R_{KO} , and the BSE maximum escape depth, T_A . These are plotted for a bulk matrix of GaN via equation 2, as a function of LE, E_0 .

approximation that describes how the BSE maximum escape depth, T_A , is related to the commonly used normalized electron range, R_{KO} , of primary electrons with LE, E_0 (Kanaya & Okayama, 1972; Niedrig & Rau, 1998):

$$T_A = \frac{R_{KO}}{2} = 0.0138 \frac{AE_0^{1.67}}{\rho Z^{0.89}}. \quad (2)$$

Here, T_A and R_{KO} are in units of μm , E_0 is in keV, ρ is the density in g/cm^3 , A is the atomic weight of the bulk material, and Z is the atomic number. Note that R_{KO} breaks down at lower LEs, but such energies are not the concern of this discussion (Joy & Luo, 1989). Figure 16 plots both T_A and R_{KO} as a function of LE for bulk GaN and illustrates how their magnitude increases with depth.

Principally, Figure 16 suggests that when imaging bulk GaN with a 20 keV LE, the normalized electron range R_{KO} could be ca. $2\ \mu\text{m}$ and subsequently, the maximum escape depth T_A could be ca. $1\ \mu\text{m}$. This extent suggests that up to ten of the porous layers in our $V_0 + 5\ \text{V}$ DBR might be visible in the BSE-SEM presented throughout this work. However, through the correlative microscopy in Figures 5 and 6, we showed that most of the image contrast relates to features in the first porous layer.

Rau & Reimer (2001) also used the following equation 3, which describes the image contrast, K , between a host material, A , and a sub-surface inhomogeneity, B :

$$K = \frac{I_A - I_B}{I_A + I_B} = \frac{\eta_A - \eta_B}{\eta_A + \eta_B} \exp\left(\frac{-4t}{T_A}\right). \quad (3)$$

For this discussion, A corresponds to GaN, and B corresponds to pores, i.e. the absence of GaN and thus treated as the vacuum. I_A and I_B denote the BSE signals from the homogeneous bulk materials A and B , respectively. When calculating the contrast between A and B , the BSE signal ratio is then expressed in terms of the relative BSE coefficients, η_A and η_B (assumed as zero), from each material, and an exponential decay component which includes both the depth, t , of B as well as the maximum escape depth.

Therefore, equation 3 suggests that image contrast can be increased in three ways: through having a significant difference in the BSE coefficients of the two materials, by the interface between the two materials being closer to the sample

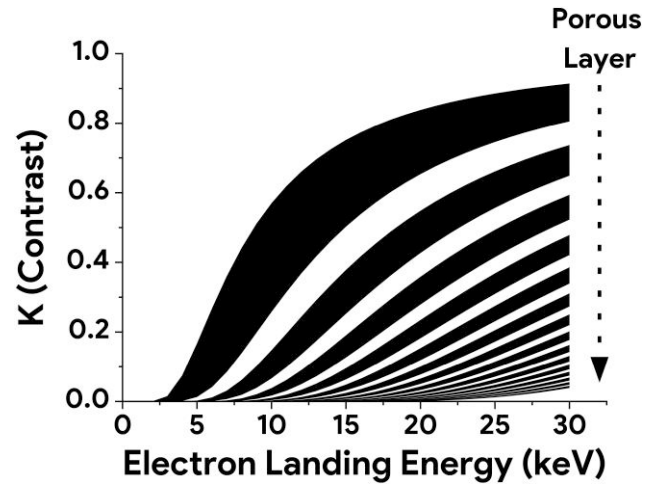


Fig. 17. Image contrast, K , plotted for a 15-pair porous GaN DBR, as described in Figure 1a, as a function of LE, E_0 . This relationship is plotted parametrically via equation 3 using depth, t , where each black stripe is a spatially descending layer of periodic porosity.

surface, and by imaging in a host material with a reduced maximum escape range. This relationship is plotted as a function of LE and depth for the 15-pair porous GaN DBR structure described in Figure 1a, where each black stripe in Figure 17 is related to a porous layer.

The first and most prominent black stripe relates to the contrast between bulk GaN and the pores in the first porous layer located 45 nm to 108 nm sub-surface. When considering a LE of 20 keV, the maximal contrast value achievable here is 0.84 at the point closest to the surface, and this contrast decays to 0.65 at the bottom of that porous layer. Between 5 keV and 10 keV, this porous layer is associated with a rapidly rising contrast (especially so for the topmost region), which then approaches a plateau for higher LEs—this corresponds to our observations and analysis of $V_0 + 5\ \text{V}$ in Figure 4.4, whereby the highest CNR was seen at 20 keV. No further improvement from the first layer was achieved by increasing the LE to 25 keV.

The cross-sectional FIB-SEM of 15-pair porous DBRs in the *Cross-sectional FIB-SEM* section highlights that multiple branching pores may be vertically stacked within a porous layer. However, the plan-view BSE-SEM presented in the *Plan-view BSE-SEM* section does not appear to reflect this, which may also result from the predicted contrast being dominated by the uppermost region of the uppermost porous layer.

The second black stripe describes the contrast in the second porous layer, 153 nm to 216 nm sub-surface. There are significant limitations on the accuracy of our approach here because equations 2 and 3 assume only bulk GaN in the material overlying the second porous layer and, therefore, do not account for imaging through regions that are a porous and non-porous mixture. Nonetheless, we once more consider the behavior at 20 keV, at the top of this porous layer; the contrast has reduced to 0.54, with a value of 0.42 towards the bottom. This second black stripe is also narrower, indicating a reduced contrast difference between the layer's top and bottom. This disparity within layers continues to decay with depth.

Whilst not a feature of the hardware available for this work, BSE energy filtering using either a cutoff value or energy windows is known to be an additional source of contrast improvement (Orlikovsky & Rau, 2011). For example, increasing the

CNR of the first porous layer of 15-pair porous DBRs may be possible by filtering out lower energy BSEs originating from regions beyond 108 nm.

The BSE-SEM of a 5-pair porous DBR presented in the *Surface, Near-surface, and Sub-surface Microscopy* section showed that porosity could be detected ca. 295 nm sub-surface, but with poor contrast. The third black stripe in Figure 17 estimates contrast for bulk GaN and pores 261–324 nm sub-surface and produces a 0.31 predicted contrast value at 295 nm, which appears consistent with this observation.

Spatial Resolution

The following discussion builds on the work by Lukiyanov et al. (2009), which considered the simple empirical or semi-empirical expressions that can be used to describe the lateral spread of penetrating primary electrons as they undergo multiple scattering through a solid matrix—in particular, Au and Al matrices were used to compare previously published models and their proposed model. Equation 4 is a commonly known expression that describes the broadening of an electron beam with a radius, r , as a function of depth, t , through a material with density, ρ , atomic weight, A , and atomic number, Z .

$$r = 0.625 \left(\frac{Z}{E_0} \right) \left(\frac{\rho}{A} \right) t^{1.5}. \quad (4)$$

The authors found that equation 4 provides a radial spread underestimation when calculating higher depth values, beyond a certain deviation point, at a fixed 20 keV LE. For Au, this deviation occurs from around 100 nm sub-surface; for Al, it occurs from around 400 nm. The ROI investigated for BSE-SEM spatial resolution quantification in the *Quantification—Spatial Resolution* section was the first porous layer with a longitudinal extent of up to 108 nm, and hence, equation 4 should be sufficient for this discussion considering that GaN has values of ρ , A , and Z that lie between those of Al and Au.

Figure 18 shows plots of radial spread, r , in bulk GaN for LE values of 10 keV, 15 keV, 20 keV, and 25 keV to mirror those in our experimental quantification. This approach allows us to consider the spread of the electron beam when it arrives at different porous layers, assuming propagation solely through bulk GaN. Overall, we see an increase in the radial spread as a function of depth and a decrease in the radial spread as a function of LE.

In the first 45 nm of material, the electron beam appears to have a relatively minimal spreading with a LE of 20 keV producing an r value of 2.2 nm. The beam continues to spread out as it travels through the material; at 108 nm of depth, the estimated value of r is now 8.1 nm. At the onset of the second porous layer, at 153 nm deep, r is now 14.3 nm, which no doubt reduces the ability to resolve nanostructure and perhaps contributes to the extent to which the top region of the topmost porous layer dominates sub-surface BSE-SEM.

Therefore, reduced beam broadening through the 45 nm GaN cap is achieved with a higher LE, consequently promoting spatial resolution as the LE is increased from 10 keV, with diminishing returns towards the 25 keV. Overall, these r estimates appear consistent with the experimental trends in increasing the LE from 10 keV to 15 keV and then to 20 keV, as set out in the *Quantification—Spatial Resolution* section.

The work set out by Probst et al. (2012) sought to optimize BSE-SEM spatial resolution through Monte Carlo simulations of a C layer 2 nm inside a Au matrix and of a Au layer 2 nm

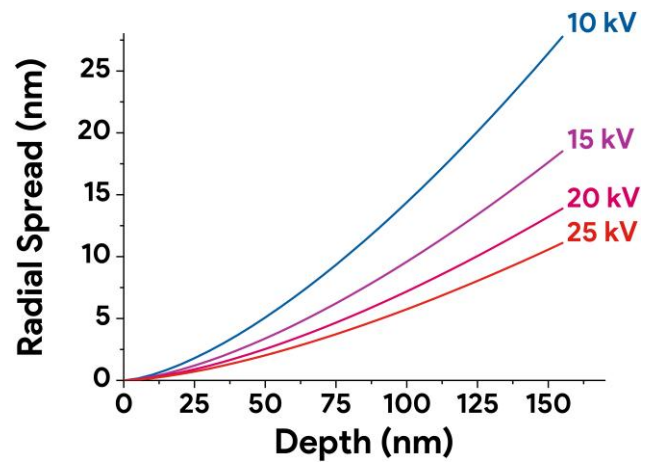


Fig. 18. Radial electron beam broadening, r , as a function of depth, t , into bulk GaN. This relationship is plotted parametrically via equation 4 for LE, E_0 , of 10 keV to 25 keV and assumes an initial electron beam diameter of zero.

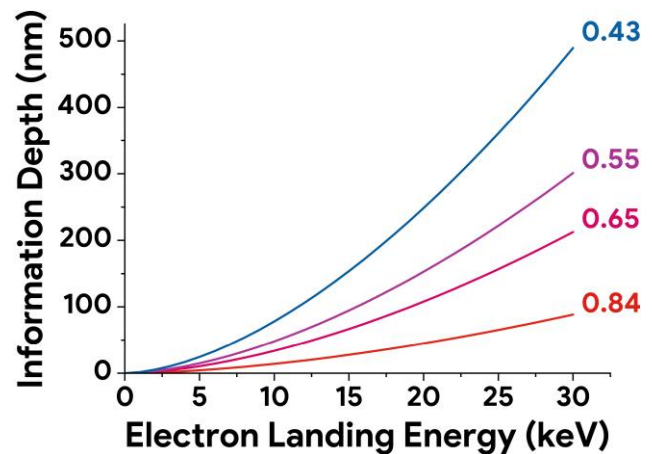


Fig. 19. Information depth as a function of LE, E_0 . This relationship is plotted parametrically via equation 5 using contrast K as calculated for values of 0.84, 0.65, 0.55, and 0.42.

inside a C matrix, at LE values of 1 keV, 10 keV, and 30 keV. They showed that one should reduce probe size to a similar extent as the features to be imaged and reduce LE for improved spatial resolution. The conventional advice to achieve nanoscale spatial resolution at the sample's surface is generally to minimize the LE in pursuit of a minimized interaction volume (Liu, 2000; Kim et al., 2010). However, our experimental observations and consideration of beam broadening in GaN suggest this does not apply to sub-surface porous nitride layers due to the required sampling depth (Čalkovský et al., 2022).

Information Depth

Österreicher et al. (2018) considered information depth in the BSE-SEM of sub-surface $\text{Al}_{12}\text{Mn}_2\text{FeSi}$ spherical nanoparticles as embedded into an Al matrix. They simulated micrographs as a function of diameter (100 nm, 250 nm, 500 nm) and LE (10 keV, 20 keV, 30 keV). The observed contrast was of bright nanoparticles against a dark background due to the Z difference. Most pertinently, the nanoparticles took on an increasingly

diffuse (reduced image contrast) and blurred (reduced spatial resolution) appearance when deeper within the Al—which corresponds to our BSE observations and FIB tomography analysis of the $V_0 + 5\text{ V}$ second porous layer in the *Correlative Microscopy* and *Tomographic FIB-SEM* sections, respectively.

The qualitative appearance of such image features has been reproduced in other papers that simulate the beam-specimen interaction using Monte Carlo approaches. In a configuration with an image contrast of bright objects against a dark background, which is analogous to the results by [Österreicher et al. \(2018\)](#), [Yue et al. \(2005\)](#) simulated line scans of Pt nanoparticles as a function of diameter (5 nm to 20 nm) and as of depth into a C host matrix (0 nm to 50 nm). These line scans were associated with reduced BSE yield and thus reduced contrast against the background, as well as a broadening of the nanoparticle peaks and thus reduced spatial resolution. In a configuration with image contrast of dark features against a bright background, which is analogous to the results in our work, simulated BSE coefficient images of spherical voids, as a function of diameter (50 to 550 nm) and as of depth (25 to 275 nm) into a Ni-based superalloy, were also associated with the same blurring of image features and degradation of contrast with depth ([Payton & Mills, 2011](#)).

A common rule of thumb invoked for the information depth is $0.5R_{KO}$ or ca. 1,000 nm in our beam-specimen configuration ([Wells, 1979](#); [Niedrig & Rau, 1998](#)). [Österreicher et al. \(2018\)](#) derived a model to describe the information depth for their configuration, using Monte Carlo simulations of electron trajectories in the material and further analysis of the obtained SNR, notably invoking the idea of a threshold SNR. It was validated through a quantitative determination of nanoparticle number density and mean diameter from experimental BSE-SEM, which showed good agreement with results from TEM, pertinently concluding that the $0.5R_{KO}$ and similar estimates are an overestimation of the information depth.

Revisiting the work of Rau and Reimer yields an information depth estimate of $0.2R_{KO}$ or ca. 400 nm in our beam-specimen configuration ([Rau & Reimer, 2001](#)). This value is also higher than that of [Österreicher et al.](#) but remains within the range of other published estimates such as $0.27R_{KO}$ or ca. 540 nm ([Piños et al., 2017](#)). They used [equation 5](#) as an estimate of the information depth, D , as a function of the LE, which includes the [equation 2](#) BSE maximum escape depth, T_A , the [equation 3](#) contrast, K , and BSE coefficients, η_A and η_B ([Niedrig & Rau, 1998](#)).

$$D = \frac{T_A}{4} \ln \left[\frac{\eta_A - \eta_B}{(\eta_A + \eta_B)K} \right]. \quad (5)$$

This relationship is plotted using K values of 0.84, 0.65, 0.55, and 0.42, which are associated with the top and bottom of the first porous layer and likewise for the second porous layer, respectively. Firstly, the information depth estimates of ca. 400 nm to 500 nm appear to include the extent of the first and second porous layers. We have shown in the *Tomographic FIB-SEM* section that the first porous layer dominates the 20 keV LE BSE-SEM of the 15-pair porous DBR $V_0 + 5\text{ V}$ but that slight local contrast modulations can be attributed to the second porous layer. Therefore, we suggest that most of our image contrast comes from higher-energy backscattered electrons undergoing a lower number of scattering events, originating closer to the surface in the incident beam vicinity.

Our inability to detect distinct layers beyond the second, when considering the information provided in both [Figure 17](#) and the experimental data presented throughout this work, suggests a threshold contrast value of ca. 0.3–0.4. Lastly, we can now estimate the “high-contrast information depth”, which for 20 keV LE is much reduced at around $0.05R_{KO}$. This approach allows us to predict optimized LE values for future imaging of porous DBRs with different cap sizes.

Conclusions

In this work, three porous GaN DBRs were fabricated via MOVPE of undoped/doped periodic multilayers, followed by ECE. This doping-selective porosification of GaN offers a non-compositional degree of freedom to adjust optoelectronic material properties. However, plan-view characterization of the sub-surface nanoscale porosity has previously relied on destructive and methodologically challenging HAADF-STEM and tomographic FIB-SEM. We presented BSE-SEM as a method for the rapid and non-destructive imaging of porous GaN DBRs. In mesoporous GaN DBRs, it revealed the same nanostructure as HAADF-STEM captured with only a fraction of the sample preparation time and microscope capital cost.

Directly correlated micrographs were obtained in the same microporous GaN DBR ROI via PeakForce Tapping AFM, SEM using in-column SE and annular BSE detectors, and tomographic FIB-SEM. These surface, near-surface, and sub-surface results revealed that in our 20 keV LE BSE-SEM approach micrographs were dominated by first porous layer features (45 nm to 108 nm sub-surface) with small, highly diffuse second layer contributions (153 to 216 nm sub-surface). Additionally, quantification of SE-SEM and BSE-SEM, as a function of LE, showed the optimized signal type and LE combination when pursuing maximal image contrast and spatial resolution in a Zeiss GeminiSEM 300 is BSE and at or near 20 keV, respectively.

The optimized BSE-SEM approach detected porosity ca. 295 nm sub-surface in an overgrown porous GaN DBR, albeit with low contrast. Imaging through a ca. 190 nm GaN cap improved contrast substantially. Such micrographs were dominated by the porosity in the uppermost porous layer with minimal influence of the layers further down, as verified through tomographic FIB-SEM. Monte Carlo simulations suggest that for a ca. 190 nm cap, one might expect contrast from at least one additional porous layer, which may explain the appearance of blurred features in addition to those resolved with high spatial resolution or contrast. These findings are consistent with the directly correlated microscopy, where some signatures of the second porous layer were observable.

Lastly, we considered expectations of image contrast, spatial resolution, and information depth derived from commonly used semi-empirical expressions in the broader literature. Sub-surface image contrast between bulk GaN and pores and spatial resolution of those pores can be improved with higher LE, but the improvements plateau at the highest energies. The image is predicted to be dominated by the uppermost porous layer’s uppermost region. Most pertinently, information depth also increases with higher LE, but its extent is reduced when limited to the high-contrast regime of BSE imaging. These findings echo the experimental analysis conducted in this article.

In conclusion, BSE-SEM can be used to image sub-surface porosity and hence will be useful in assessing the impact of

changing etch conditions on the sub-surface pore morphology in a rapid and non-destructive manner, which can be used to assess relatively large plan-view material areas. We also note that we have successfully imaged a range of GaN samples using these imaging conditions with different porous morphologies owing to disparities in epitaxial structure, electrochemical etching potential, chemical species, defect type, and density but with similar cap thicknesses. Lastly, we expect this imaging approach to apply to samples etched via a lithographic trench approach. Our insights into sub-surface imaging in porous nitrides are also relevant to imaging of other porous and, indeed, composite materials.

Availability of Data and Materials

The authors have declared that no datasets apply for this piece.

Supplementary Material

To view supplementary material for this article, please visit <http://academic.oup.com/mam/article-lookup/doi/10.1093/mam/ozae028#supplementary-data>.

Acknowledgments

Maruf Sarkar would like to thank Simon Griggs (Wolfson Electron Microscopy Suite, Department of Materials Science and Metallurgy, University of Cambridge) for technical support.

Financial Support

This work was supported by the UK under Grant Nos. EP/N509620/1, EP/R513180/1, and EP/R03480X/1. Maruf Sarkar would also like to acknowledge funding from The Armourers and Brasiers' Gauntlet Trust. Rachel Oliver would like to acknowledge funding from the Royal Academy of Engineering under the Chairs in Emerging Technologies Scheme, which is sponsored by the Department for Science, Innovation and Technology (DSIT).

Conflict of Interest

No competing interest is declared.

References

- Abe H, Babin S, Borisov S, Hamaguchi A, Kadowaki M, Miyano Y & Yamazaki Y (2009). Contrast reversal effect in scanning electron microscopy due to charging. *J Vac Sci; Technol B: Microelectron Nanometer Struct* 27(3), 1039. <https://doi.org/10.1116/1.3114486>
- Ando T, Bhamidimarri SP, Brending N, Colin-York H, Collinson L, De Jonge N, de Pablo PJ, Debroye E, Egging C, Franck C, Fritzsche M, Gerritsen H, Giepmans BNG, Grunewald K, Hofkens J, Hoogenboom JP, Janssen KPF, Kaufman R, Klumpermann J, Kurniawan N, Kusch J, Liv N, Parekh V, Peckys DB, Rehfeldt F, Reutens DC, Roeffaers MJB, Salditt T, Schaap IAT, Schwarz US, Verkade P, Vogel MW, Wagner R, Winterhalter M, Yuan H & Zifarelli G (2018). The 2018 correlative microscopy techniques roadmap. *J Phy D: Appl Phys* 51(44), 443001. <https://doi.org/10.1088/1361-6463/aad055>
- Bergin M, Ward D, Ellis J & Jardine A (2019). A method for constrained optimisation of the design of a scanning helium microscope. *Ultramicroscopy* 207, 112833. <https://doi.org/10.1016/j.ultramicro.2019.112833>
- Čalkovský M, Müller E & Gerthsen D (2022). Quantitative analysis of backscattered-electron contrast in scanning electron microscopy. *J Microsc* 289(1), 32–47. <https://doi.org/10.1111/jmi.v289.1>
- Cantoni M & Holzer L (2014). Advances in 3D focused ion beam tomography. *MRS Bull* 39(4), 354–360. <https://doi.org/10.1557/mrs.2014.54>
- Cazaux J (2012). From the physics of secondary electron emission to image contrasts in scanning electron microscopy. *J Electron Microsc* 61(5), 261–284. <https://doi.org/10.1093/jmicro/dfs048>
- Chen D, Xiao H & Han J (2012). Nanopores in GaN by electrochemical anodization in hydrofluoric acid: Formation and mechanism. *J Appl Phys* 112(6), 064303. <https://doi.org/10.1063/1.4752259>
- Cizmar P, Vladár AE, Ming B & Postek MT (2008). Simulated SEM images for resolution measurement. *Scanning* 30(5), 381–391. <https://doi.org/10.1002/sca.v30.5>
- Crouzier L, Delvallée A, Devoille L, Artous S, Saint-Antonin F & Feltin N (2021). Influence of electron landing energy on the measurement of the dimensional properties of nanoparticle populations imaged by SEM. *Ultramicroscopy* 226, 113300. <https://doi.org/10.1016/j.ultramicro.2021.113300>
- Drouin D, Couture AR, Joly D, Tastet X, Aimez V & Gauvin R (2007). CASINO V2.42—a fast and easy-to-use modeling tool for scanning electron microscopy and microanalysis users. *Scanning* 29(3), 92–101. <https://doi.org/10.1002/sca.v29.3>
- Elafandy RT, Kang J -H, Mi C, Kim TK, Kwak JS & Han J (2021). Study and application of birefringent nanoporous GaN in the polarization control of blue vertical-cavity surface-emitting lasers. *ACS Photonics* 8(4), 1041–1047. <https://doi.org/10.1021/acsp Photonics.1c00211>
- Fager C, Röding M, Olsson A, Lorén N, von Corswant C, Särkkä A & Olsson E (2020). Optimization of FIB-SEM tomography and reconstruction for soft, porous, and poorly conducting materials. *Microsc Microanal* 26(4), 837–845. <https://doi.org/10.1017/S1431927620001592>
- Garitagoitia Cid A, Rosenkranz R, Löffler M, Clausner A, Standke Y & Zschech E (2018). Quantitative analysis of backscattered electron (BSE) contrast using low voltage scanning electron microscopy (LVSEM) and its application to Al_{0.22}Ga_{0.78}N/GaN layers. *Ultramicroscopy* 195, 47–52. <https://doi.org/10.1016/j.ultramicro.2018.08.026>
- Giannuzzi LA & Stevie FA (2010). *Introduction to Focused Ion Beams Instrumentation, Theory, Techniques and Practice*. New York, NY: Springer.
- Goldstein JI, Newbury DE, Michael JR, Ritchie NW, Scott JH & Joy DC (2017). *Scanning Electron Microscopy and X-Ray Microanalysis*. New York, NY: Springer.
- Griffin PH, Frentrup M, Zhu T, Vickers ME & Oliver RA (2019). Structural characterization of porous GaN distributed Bragg reflectors using x-ray diffraction. *J Appl Phys* 126(21), 213109. <https://doi.org/10.1063/1.5134143>
- Griffin PH & Oliver RA (2020). Porous nitride semiconductors reviewed. *J Phys D: Appl Phys* 53(38), 383002. <https://doi.org/10.1088/1361-6463/ab9570>
- Griffin PH, Patel KM, Zhu T, Langford RM, Kamboj VS, Ritchie DA & Oliver RA (2020). The relationship between the three-dimensional structure of porous GaN distributed Bragg reflectors and their birefringence. *J Appl Phys* 127(19), 193101. <https://doi.org/10.1063/5.0005770>
- Griffin P, Zhu T & Oliver R (2018). Porous AlGaIn-based ultraviolet distributed Bragg reflectors. *Materials* 11(9), 1487. <https://doi.org/10.3390/ma11091487>
- Heo J, Kim J, Jeong T, Lee S, Ihn YS, Kim Z & Jo Y (2022). Lossy and noisy channel simulation in computational ghost imaging by using noise-induced pattern. *Sci Rep* 12(1), 11787. <https://doi.org/10.1038/s41598-022-15783-6>
- Jaksch H & Martin JP (1995). High-resolution, low-voltage SEM for true surface imaging and analysis. *Fresenius J Anal Chem* 353(3–4), 378–382. <https://doi.org/10.1007/s0021653530378>

- Jarman JC, Zhu T, Griffin PH & Oliver RA (2019). Light-output enhancement of InGaN light emitting diodes regrown on nanoporous distributed Bragg reflector substrates. *Jpn J Appl Phys* 58(SC), SCCC14. <https://doi.org/10.7567/1347-4065/ab0cfd>
- Jiang X, Zhang T, Xu L, Wang C, Zhou X & Gu N (2011). Surfactant-induced formation of honeycomb pattern on micropipette with curvature gradient. *Langmuir* 27(9), 5410–5419. <https://doi.org/10.1021/la200375t>
- Jönsson M & Björk G (2020). Contrast resolution of few-photon detectors. *J Phys Photonics* 2(4), 045008. <https://doi.org/10.1088/2515-7647/ababf6>
- Joy DC & Luo S (1989). An empirical stopping power relationship for low-energy electrons. *Scanning* 11(4), 176–180. <https://doi.org/10.1002/sca.v11.4>
- Kanaya K & Okayama S (1972). Penetration and energy-loss theory of electrons in solid targets. *J Phys D: Appl Phys* 5(1), 43–58. <https://doi.org/10.1088/0022-3727/5/1/308>
- Ke Y, Wang C-J, Hsieh Y-S, Shiu G-Y, Kao Y-C, Chen K-T, Chen H, Han J & Lin C-F (2023). Cavity mode-matching InGaN aperture-emitting device with a nanoporous GaN reflector via ion implantation. *ACS Appl Opt Mater* 1(7), 1326–1331. <https://doi.org/10.1021/acsaom.3c00152>
- Kim H, Negishi T, Kudo M, Takei H & Yasuda K (2010). Quantitative backscattered electron imaging of field emission scanning electron microscopy for discrimination of nano-scale elements with nm-order spatial resolution. *J Electron Microsc* 59(5), 379–385. <https://doi.org/10.1093/jmicro/dfq012>
- Kumagai K & Sekiguchi T (2009). Sharing of secondary electrons by in-lens and out-lens detector in low-voltage scanning electron microscope equipped with immersion lens. *Ultramicroscopy* 109(4), 368–372. <https://doi.org/10.1016/j.ultramic.2009.01.005>
- Kwong W & Zhang W (2005). Electron-beam assisted platinum deposition as a protective layer for FIB and TEM applications. In *ISSM 2005, IEEE International Symposium on Semiconductor Manufacturing 2005*, San Jose, CA, USA, pp. 469–471. IEEE. <https://doi.org/10.1109/ISSM.2005.1513408>
- Lee S-M, Gong S-H, Kang J-H, Ebaid M, Ryu S-W & Cho Y-H (2015). Optically pumped GaN vertical cavity surface emitting laser with high index-contrast nanoporous distributed Bragg reflector. *Opt Express* 23(9), 11023. <https://doi.org/10.1364/OE.23.011023>
- Liu J (2000). High-resolution and low-voltage FE-SEM imaging and microanalysis in materials characterization. *Mater Charact* 44(4-5), 353–363. [https://doi.org/10.1016/S1044-5803\(99\)00076-5](https://doi.org/10.1016/S1044-5803(99)00076-5)
- Liu J, Liu D, Shen Y, Yang X, Zhao C, Chen R, Yang Z, Liu J, Ma J & Xiao H (2020). Fabrication and applications of wafer-scale nanoporous GaN near-infrared distributed Bragg reflectors. *Opt Mater (Amst)* 107, 110093. <https://doi.org/10.1016/j.optmat.2020.110093>
- Lukyanov FA, Rau EI & Sennov RA (2009). Depth range of primary electrons, electron beam broadening, and spatial resolution in electron-beam studies. *Bull Russ Acad Sci Phys* 73(4), 441–449. <https://doi.org/10.3103/S1062873809040029>
- Makovetsky R, Piche N & Marsh M (2018). Dragonfly as a platform for easy image-based deep learning applications. *Microsc Microanal* 24(S1), 532–533. <https://doi.org/10.1017/S143192761800315X>
- Massabuau FC-P, Griffin PH, Springbett HP, Liu Y, Kumar RV, Zhu T & Oliver RA (2020a). Dislocations as channels for the fabrication of sub-surface porous GaN by electrochemical etching. *APL Mater* 8(3), 031115. <https://doi.org/10.1063/1.5142491>
- Massabuau FC-P, Springbett H, Divitini G, Griffin P, Zhu T & Oliver R (2020b). Sequential plan-view imaging of sub-surface structures in the transmission electron microscope. *Materialia* 12, 100798. <https://doi.org/10.1016/j.mtl.2020.100798>
- Mays T (2007). A new classification of pore sizes. *Stud Surf Sci Catal* 160, 57–62. [https://doi.org/10.1016/S0167-2991\(07\)80009-7](https://doi.org/10.1016/S0167-2991(07)80009-7)
- Mishkat-UL-Masabih S, Luk TS, Rishinaramangalam A, Monavian M, Nami M & Feezell D (2018). Nanoporous distributed Bragg reflectors on free-standing nonpolar m-plane GaN. *Appl Phys Lett* 112(4), 041109. <https://doi.org/10.1063/1.5016083>
- Niedrig H & Rau E (1998). Information depth and spatial resolution in BSE microtomography in SEM. *Nucl Instrum Methods Phys Res Sec B: Beam Interact Mater At* 142(4), 523–534. [https://doi.org/10.1016/S0168-583X\(98\)00318-8](https://doi.org/10.1016/S0168-583X(98)00318-8)
- O’Hanlon T, Bao A, Massabuau F-P, Kappers M & Oliver R (2020). Cross-shaped markers for the preparation of site-specific transmission electron microscopy lamellae using focused ion beam techniques. *Ultramicroscopy* 212, 112970. <https://doi.org/10.1016/j.ultramic.2020.112970>
- Oliver R, Kappers M, Sumner J, Datta R & Humphreys C (2006). Highlighting threading dislocations in MOVPE-grown GaN using an in situ treatment with SiH₄ and NH₃. *J Cryst Growth* 289(2), 506–514. <https://doi.org/10.1016/j.jcrysgro.2005.12.075>
- Orlikovsky NA & Rau EI (2011). Image contrast in the backscattered electron mode in scanning electron microscopy and microtomography. *Bull Russ Acad Sci Phys* 75(9), 1234–1239. <https://doi.org/10.3103/S1062873811090218>
- Österreicher JA, Grabner F, Schiffl A, Schwarz S & Bourret GR (2018). Information depth in backscattered electron microscopy of nanoparticles within a solid matrix. *Mater Charact* 138, 145–153. <https://doi.org/10.1016/j.matchar.2018.01.049>
- Palmquist NC, Anderson R, Kearns JA, Back J, Trageser E, Gee S, Denbaars SP & Nakamura S (2023). Long-cavity M-plane GaN-based vertical-cavity surface-emitting lasers with a topside monolithic curved mirror. *Photonics* 10(6), 646. <https://doi.org/10.3390/photonics10060646>
- Park J, Kang J-H & Ryu S-W (2013). High diffuse reflectivity of nanoporous GaN distributed Bragg reflector formed by electrochemical etching. *Appl Phys Express* 6(7), 072201. <https://doi.org/10.7567/APEX.6.072201>
- Payton E & Mills M (2011). Stereology of backscatter electron images of etched surfaces for characterization of particle size distributions and volume fractions: Estimation of imaging bias via Monte Carlo simulations. *Mater Charact* 62(6), 563–574. <https://doi.org/10.1016/j.matchar.2011.04.003>
- Piños J, Mikmeková S & Frank L (2017). About the information depth of backscattered electron imaging. *J Microsc* 266(3), 335–342. <https://doi.org/10.1111/jmi.12542>
- Pittenger B, Erina N & Su C (2010). Quantitative mechanical property mapping at the nanoscale with PeakForce QNM. *Bruker*.
- Probst C, Demers H & Gauvin R (2012). Spatial resolution optimization of backscattered electron images using Monte Carlo simulation. *Microsc Microanal* 18(3), 628–637. <https://doi.org/10.1017/S1431927612000207>
- Rau EI & Reimer L (2001). Fundamental problems of imaging subsurface structures in the backscattered electron mode in scanning electron microscopy. *Scanning* 23(4), 235–240. <https://doi.org/10.1002/sca.v23.4>
- Reimers IA, Safonov IV & Yakimchuk IV (2019). Segmentation of 3D FIB-SEM data with pore-back effect. *J Phys: Conf Ser* 1368(3), 032015. <https://doi.org/10.1088/1742-6596/1368/3/032015>
- Schindelin J, Arganda-Carreras I, Frise E, Kaynig V, Longair M, Pietzsch T, Preibisch S, Rueden C, Saalfeld S, Schmid B, Tinevez J-Y, White DJ, Hartenstein V, Eliceiri K, Tomancak P & Cardona A (2012). Fiji: An open-source platform for biological-image analysis. *Nat Methods* 9(7), 676–682. <https://doi.org/10.1038/nmeth.2019>
- Serafińczuk J, Moszak K, Pawlaczyk Ł, Olszewski W, Pucicki D, Kudrawiec R & Hommel D (2020). Determination of dislocation density in GaN/sapphire layers using XRD measurements carried out from the edge of the sample. *J Alloys Compd* 825, 153838. <https://doi.org/10.1016/j.jallcom.2020.153838>
- Shiojiri M, Chuo CC, Hsu JT, Yang JR & Saijo H (2006). Structure and formation mechanism of V defects in multiple InGaN/GaN quantum well layers. *J Appl Phys* 99(7), 073505. <https://doi.org/10.1063/1.2180532>
- Shiu G-Y, Chen K-T, Fan F-H, Huang K-P, Hsu W-J, Dai J-J, Lai C-F & Lin C-F (2016). InGaN light-emitting diodes with an embedded

- nanoporous GaN distributed Bragg reflectors. *Sci Rep* 6(1), 29138. <https://doi.org/10.1038/srep29138>
- Springbett HP, Gao K, Jarman J, Zhu T, Holmes M, Arakawa Y & Oliver RA (2018). Improvement of single photon emission from InGaN QDs embedded in porous micropillars. *Appl Phys Lett* 113(10), 101107. <https://doi.org/10.1063/1.5045843>
- Su C, Shi J, Hu Y, Hu S & Ma J (2016). Method and apparatus of using peak force tapping mode to measure physical properties of a sample. US9291640B2.
- Tandokoro K, Nagoshi M, Kawano T, Sato K & Tsuno K (2018). Low-voltage SEM contrasts of steel surface studied by observations and electron trajectory simulations for GEMINI lens system. *Microscopy* 67(5), 274–279. <https://doi.org/10.1093/jmicro/dfy030>
- Thevenaz P, Ruttimann U & Unser M (1998). A pyramid approach to subpixel registration based on intensity. *IEEE Trans Image Process* 7(1), 27–41. <https://doi.org/10.1109/83.650848>
- Timischl F (2014). The contrast-to-noise ratio for image quality evaluation in scanning electron microscopy. *Scanning* 37(1), 54–62. <https://doi.org/10.1002/sca.v37.1>
- Tseng WJ, van Dorp DH, Lieten RR, Vereecken PM & Borghs G (2014). Anodic etching of n-GaN epilayer into porous GaN and its photoelectrochemical properties. *J Phys Chem C* 118(51), 29492–29498. <https://doi.org/10.1021/jp508314q>
- Volkert CA & Minor AM (2007). Focused ion beam microscopy and micromachining. *MRS Bull* 32(5), 389–399. <https://doi.org/10.1557/mrs2007.62>
- Wei B, Han Y, Wang Y, Zhao H, Sun B, Yang X, Han L, Wang M, Li Z, Xiao H & Zhang Y (2020). Tunable nanostructured distributed Bragg reflectors for III-nitride optoelectronic applications. *RSC Adv* 10(39), 23341–23349. <https://doi.org/10.1039/D0RA03569F>
- Wells OC (1979). Effects of collector take-off angle and energy filtering on the BSE image in the SEM. *Scanning* 2(4), 199–216. <https://doi.org/10.1002/sca.v2:4>
- Welvaert M & Rosseel Y (2013). On the definition of signal-to-noise ratio and contrast-to-noise ratio for fMRI data. *PLoS One* 8(11), e77089. <https://doi.org/10.1371/journal.pone.0077089>
- Wünsche J, Cardenas L, Rosei F, Cicoira F, Gauvin R, Graeff CF, Poulin S, Pezzella A & Santato C (2013). In situ formation of dendrites in eumelanin thin films between gold electrodes. *Adv Funct Mater* 23(45), 5591–5598. <https://doi.org/10.1002/adfm.201300715>
- Xu CS, Hayworth KJ, Lu Z, Grob P, Hassan AM, García-Cerdán JG, Niyogi KK, Nogaes E, Weinberg RJ & Hess HF (2017). Enhanced FIB-SEM systems for large-volume 3D imaging. *eLife* 6, e25916. <https://doi.org/10.7554/eLife.25916>
- Yang X, Chen Z, Cao D, Zhao C, Shen L, Luan C, Pang Z, Liu J, Ma J & Xiao H (2019). Large-area, liftoff nanoporous GaN distributed Bragg reflectors: Fabrication and application. *Appl Surf Sci* 489, 849–855. <https://doi.org/10.1016/j.apsusc.2019.05.128>
- Yao Y, Liang Y, Guo J & Xiu H (2023). The development and applications of nanoporous gallium nitride in optoelectronics: A review. *Semicond Sci Technol* 38(7), 074001. <https://doi.org/10.1088/1361-6641/accd14>
- Yue YT, Li HM & Ding ZJ (2005). Monte Carlo simulation of secondary electron and backscattered electron images for a nanoparticle-matrix system. *J Phys D: Appl Phys* 38(12), 1966–1977. <https://doi.org/10.1088/0022-3727/38/12/017>
- Zeiss (2013). Instruction manual BSD4 detector. https://asset-downloads.zeiss.com/catalogs/download/mic/80a1e444-cf64-4d95-b6cb-93c283ce10b3/EN_IM_BSD4_detector_V01.pdf
- Zhang C, Park SH, Chen D, Lin D-W, Xiong W, Kuo H-C, Lin C-F, Cao H & Han J (2015). Mesoporous GaN for photonic engineering—highly reflective GaN mirrors as an example. *ACS Photonics* 2(7), 980–986. <https://doi.org/10.1021/acsphotonics.5b00216>
- Zhang B, Zhang Z & Jin C (2023). Imaging mechanism and contrast separation in low-voltage scanning electron microscopy imaging of carbon nanotube arrays on SiO₂/Si substrate. *Carbon* 213, 118175. <https://doi.org/10.1016/j.carbon.2023.118175>
- Zhao Y, Shan M, Zheng Z, Jian P, Liu W, Tan S, Chen C, Wu F & Dai J (2022). Fabrication of wafer-scale nanoporous AlGaIn-based deep ultraviolet distributed Bragg reflectors via one-step selective wet etching. *Sci Rep* 12(1), 22434. <https://doi.org/10.1038/s41598-022-25712-2>
- Zhao C, Yang X, Wei B, Liu J, Chen R, Luan C & Xiao H (2020). Enhancement in light-emission efficiency of InGaIn/GaN multiple quantum well layer by a porous-GaN mirror. *Vacuum* 182, 109669. <https://doi.org/10.1016/j.vacuum.2020.109669>
- Zhong XL, Haigh SJ, Zhou X & Withers PJ (2020). An in-situ method for protecting internal cracks/pores from ion beam damage and reducing curtaining for TEM sample preparation using FIB. *Ultramicroscopy* 219, 113135. <https://doi.org/10.1016/j.ultramic.2020.113135>
- Zhu T, Liu Y, Ding T, Fu WY, Jarman J, Ren CX, Kumar RV & Oliver RA (2017). Wafer-scale fabrication of non-polar mesoporous GaN distributed Bragg reflectors via electrochemical porosification. *Sci Rep* 7(1), 45344. <https://doi.org/10.1038/srep45344>